



A GRANULAR-BASED APPROACH TO THE ACOUSTIC PROPERTIES OF MARINE SEDIMENTS

Title	A GRANULAR-BASED APPROACH TO THE ACOUSTIC PROPERTIES OF MARINE SEDIMENTS
Item Type	Thesis
Authors	Swartz, Andrew J.
URI	https://hdl.handle.net/10945/72275
Publisher	Monterey, CA; Naval Postgraduate School
Date Issued	2023-06
Rights	This publication is a work of the U.S. Government as defined in Title 17, United States Code, Section 101. Copyright protection is not available for this work in the United States.
Download date	2026-04-14 06:02:35
Link to Item	https://hdl.handle.net/10945/72275

Downloaded from NPS Archive: Calhoun



**NAVAL
POSTGRADUATE
SCHOOL**

MONTEREY, CALIFORNIA

THESIS

**A GRANULAR-BASED APPROACH TO THE ACOUSTIC
PROPERTIES OF MARINE SEDIMENTS**

by

Andrew J. Swartz

June 2023

Thesis Advisor:

Co-Advisor:

Abram H. Clark IV

Derek Olson

Approved for public release. Distribution is unlimited.

THIS PAGE INTENTIONALLY LEFT BLANK

REPORT DOCUMENTATION PAGE			<i>Form Approved OMB No. 0704-0188</i>
Public reporting burden for this collection of information is estimated to average 1 hour per response, including the time for reviewing instruction, searching existing data sources, gathering and maintaining the data needed, and completing and reviewing the collection of information. Send comments regarding this burden estimate or any other aspect of this collection of information, including suggestions for reducing this burden, to Washington headquarters Services, Directorate for Information Operations and Reports, 1215 Jefferson Davis Highway, Suite 1204, Arlington, VA 22202-4302, and to the Office of Management and Budget, Paperwork Reduction Project (0704-0188) Washington, DC, 20503.			
1. AGENCY USE ONLY (Leave blank)	2. REPORT DATE June 2023	3. REPORT TYPE AND DATES COVERED Master's thesis	
4. TITLE AND SUBTITLE A GRANULAR-BASED APPROACH TO THE ACOUSTIC PROPERTIES OF MARINE SEDIMENTS		5. FUNDING NUMBERS RPK7Q	
6. AUTHOR(S) Andrew J. Swartz			
7. PERFORMING ORGANIZATION NAME(S) AND ADDRESS(ES) Naval Postgraduate School Monterey, CA 93943-5000		8. PERFORMING ORGANIZATION REPORT NUMBER	
9. SPONSORING / MONITORING AGENCY NAME(S) AND ADDRESS(ES) Office of Naval Research, Arlington, VA 22203		10. SPONSORING / MONITORING AGENCY REPORT NUMBER	
11. SUPPLEMENTARY NOTES The views expressed in this thesis are those of the author and do not reflect the official policy or position of the Department of Defense or the U.S. Government.			
12a. DISTRIBUTION / AVAILABILITY STATEMENT Approved for public release. Distribution is unlimited.		12b. DISTRIBUTION CODE A	
13. ABSTRACT (maximum 200 words) Understanding and predicting the acoustic behavior of water-saturated marine sediment is fundamental to underwater sensing, navigation, and communication. Data collected from experiments and field measurements show a clear dependence on frequency for both the attenuation coefficient and phase speed. Existing theories, like Biot-Stoll and VGS, can be fit to this data by fitting multiple parameter values that can be difficult to interpret or measure. Additionally, these theories treat the sediment as a continuum. We take a granular-mechanics approach, treating the medium as a large collection of spatially disordered, discrete objects governed by pairwise forces. These forces include a repulsive term due to intergrain contact forces as well as a variety of dissipative forces, including an inelastic component of normal compression at grain-grain contacts that is not included in the existing models of sediment acoustics. Using theoretical analysis and discrete element method simulations, we show that this granular mechanics perspective may be able to explain salient features of the acoustic properties of marine sediments, such as the frequency-dependent phase speed and attenuation. Our results show a granular mechanics perspective may be able to simplify our understanding of sediment acoustics and provide new insights about the grain-scale origins of observed data.			
14. SUBJECT TERMS granular mechanics, acoustics, MATLAB, simulation		15. NUMBER OF PAGES 65	
		16. PRICE CODE	
17. SECURITY CLASSIFICATION OF REPORT Unclassified	18. SECURITY CLASSIFICATION OF THIS PAGE Unclassified	19. SECURITY CLASSIFICATION OF ABSTRACT Unclassified	20. LIMITATION OF ABSTRACT UU

NSN 7540-01-280-5500

Standard Form 298 (Rev. 2-89)
Prescribed by ANSI Std. Z39-18

THIS PAGE INTENTIONALLY LEFT BLANK

Approved for public release. Distribution is unlimited.

**A GRANULAR-BASED APPROACH TO THE ACOUSTIC PROPERTIES
OF MARINE SEDIMENTS**

Andrew J. Swartz
Lieutenant, United States Navy
BSEE, Georgia Institute of Technology, 2016

Submitted in partial fulfillment of the
requirements for the degree of

MASTER OF SCIENCE IN APPLIED PHYSICS

from the

**NAVAL POSTGRADUATE SCHOOL
June 2023**

Approved by: Abram H. Clark IV
Advisor

Derek Olson
Co-Advisor

Frank A. Narducci
Chair, Department of Physics

THIS PAGE INTENTIONALLY LEFT BLANK

ABSTRACT

Understanding and predicting the acoustic behavior of water-saturated marine sediment is fundamental to underwater sensing, navigation, and communication. Data collected from experiments and field measurements show a clear dependence on frequency for both the attenuation coefficient and phase speed. Existing theories, like Biot-Stoll and VGS, can be fit to this data by fitting multiple parameter values that can be difficult to interpret or measure. Additionally, these theories treat the sediment as a continuum. We take a granular-mechanics approach, treating the medium as a large collection of spatially disordered, discrete objects governed by pairwise forces. These forces include a repulsive term due to intergrain contact forces as well as a variety of dissipative forces, including an inelastic component of normal compression at grain-grain contacts that is not included in the existing models of sediment acoustics. Using theoretical analysis and discrete element method simulations, we show that this granular mechanics perspective may be able to explain salient features of the acoustic properties of marine sediments, such as the frequency-dependent phase speed and attenuation. Our results show a granular mechanics perspective may be able to simplify our understanding of sediment acoustics and provide new insights about the grain-scale origins of observed data.

THIS PAGE INTENTIONALLY LEFT BLANK

Table of Contents

1	Introduction and Background	1
1.1	Measurements of Dispersion and Attenuation	1
1.2	Biot-Stoll Model	4
1.3	Buckingham Model	5
1.4	Sediment Acoustics as a Granular Mechanics Problem	6
1.5	Conclusion.	10
2	Theory	11
2.1	One Dimensional Theory	11
2.2	Connecting to Physical Parameters	16
2.3	Conclusion.	18
3	Simulation Methodology	19
3.1	Inputs and Setup	19
3.2	Simulation Integration Scheme	24
3.3	Simulation Driving	25
3.4	Conclusion.	27
4	Data Processing and Results	29
4.1	One Dimension Data Extraction	29
4.2	One Dimensional Results	32
4.3	Two Dimension Data Extraction	33
4.4	Two Dimension Results	34
4.5	Conclusions	38
5	Conclusions	39
5.1	Future Work	39
5.2	Closing Remarks	41

List of References	43
Initial Distribution List	49

List of Figures

Figure 1.1	Real-World Sound Speed Data vs. Biot Model	2
Figure 1.2	Real-World Attenuation Data vs. Biot Model	3
Figure 1.3	Robert Stoll’s Plot of Laboratory and Field Data for Attenuation Dispersion Relation with Biot Theory	4
Figure 1.4	Buckingham’s VGS and GS Theories Plotted against Select Laboratory Data.	6
Figure 1.5	Non-Affine Motion of Grains	7
Figure 1.6	Grain-Grain Contact Breaking	8
Figure 1.7	Branching of Force Chains	9
Figure 2.1	Darkfield Photo-Elasticity, Highlighting Force Chains in a Collection of Grains	12
Figure 2.2	One Dimensional Chain of Identical Grains	13
Figure 2.3	Real World Speed Data vs. 1D Theory	15
Figure 2.4	Real World Attenuation Data vs. 1D Theory	15
Figure 3.1	Small One Dimensional Chain of Grains	20
Figure 3.2	Over Pressurized Packing of Grains in Two Dimensions	23
Figure 3.3	Under Pressurized Packing of Grains in Two Dimensions	23
Figure 3.4	Plot of Grain Displacement for Continuously Driven Chain of Grains	26
Figure 3.5	Snapshots of Gaussian Pulsed Waveform Displacement at Four different times with Peak Tracking.	28
Figure 4.1	Log Plot of Peak Positions Tracked Through Simulation	30

Figure 4.2	Calculated Wave Speed vs. Particle Number for Gaussian Pulsed Simulation	31
Figure 4.3	Particle Displacement vs. Time for Two Particles in Same Simulation	32
Figure 4.4	Attenuation Results vs. Theory for 1 Dimension Simulations . . .	33
Figure 4.5	Wave Speed Results vs. Theory for 1 Dimension Simulations . .	34
Figure 4.6	Snapshot of Simulation for Overpressurized System	35
Figure 4.7	Snapshot of Simulation for Underpressurized System	36
Figure 4.8	Attenuation Results for 2D Simulations	37
Figure 4.9	Dispersion Results for 2D Simulations	37
Figure 5.1	Particle Positions vs. Time in 2D Simulations	40
Figure 5.2	Particle Displacement Amplitudes vs. Initial Positions	40

List of Tables

Table 2.1	Parameter Values	16
-----------	----------------------------	----

THIS PAGE INTENTIONALLY LEFT BLANK

Acknowledgments

A huge thank you to Dr. Abe Clark and Dr. Derek Olson for their support and guidance on this project, and throughout the entirety of my degree program.

To my wonderful wife, Anna, thank you for tolerating Monterey for two years and all of the stress that NPS added into our lives. Here's to the next adventure.

THIS PAGE INTENTIONALLY LEFT BLANK

CHAPTER 1:

Introduction and Background

Having a complete understanding of the marine environment is a vital to U.S. Naval operations. Of particular importance is understanding the propagation of acoustic waves, which are used for a wide variety of communication and sensing applications [1]–[13]. These applications necessarily involve modeling of how acoustic waves transmit and reflect off of water-saturated sediments at the bottom of the ocean floor. Understanding reflection and transmission requires an acoustic model of the material, complete with a dispersion relation (frequency dependence of sound speed) as well as frequency dependence of attenuation. This frequency dependence of speed and attenuation arises from microscopic loss mechanisms, and a complete theory should be able to derive this dependence in terms of one or many loss mechanisms. As discussed below, two major theories exist, but both treat the granular phase in a continuum way. This thesis will consider a new model for how acoustic waves propagate through marine sediment by explicitly focusing on the granular phase.

1.1 Measurements of Dispersion and Attenuation

It is difficult to collect data on dispersion relations in marine sediment for several reasons. Lab experiments are challenging particularly for long wavelength cases as length scales need to be longer than several wavelengths of the signal being tested. Additionally, complex inversion techniques are necessary to convert measurable data into something that can be used to determine attenuation and dispersion relations [14]. Field experiments are difficult as the material properties of sediments often change with depth on a characteristic scale of 10^{-1} m. Given this, it can be difficult to disentangle the effect of the layering structure with the dispersion relation, since layered sediments are known to cause dispersion on a macroscopic scale [15], [16]. Acoustic transmission properties can also be inferred based on reflection data collected near the ocean floor [11], [17]–[19]. With these caveats, we will primarily consider the data set from a 2007 paper [14], which showed data from several sources compiled into a single plot. The study used data from 20 locations in the Yellow Sea, East China Sea, and off the Eastern U.S. coast and ultimately produced two important graphs shown in Figures 1.1 and 1.2. The colored points in these figures symbolize the data,

with the dotted lines representing a model that will be discussed in Section 1.2.

These figures show the frequency dependence of the sound speed ratio (or the dispersion relation) and attenuation coefficient for a marine sediment. The attenuation coefficient and wave speed arising from the standard equation for a decaying plane wave.

$$u(x, t) = Ae^{-\alpha x} e^{i(kx - \omega t)}, \quad (1.1)$$

From this equation we can directly get the attenuation coefficient α , the wave number, k , and the frequency, ω . From there, the wave number and frequency can then be used to get the wave speed.

$$c = \frac{\omega}{k} \quad (1.2)$$

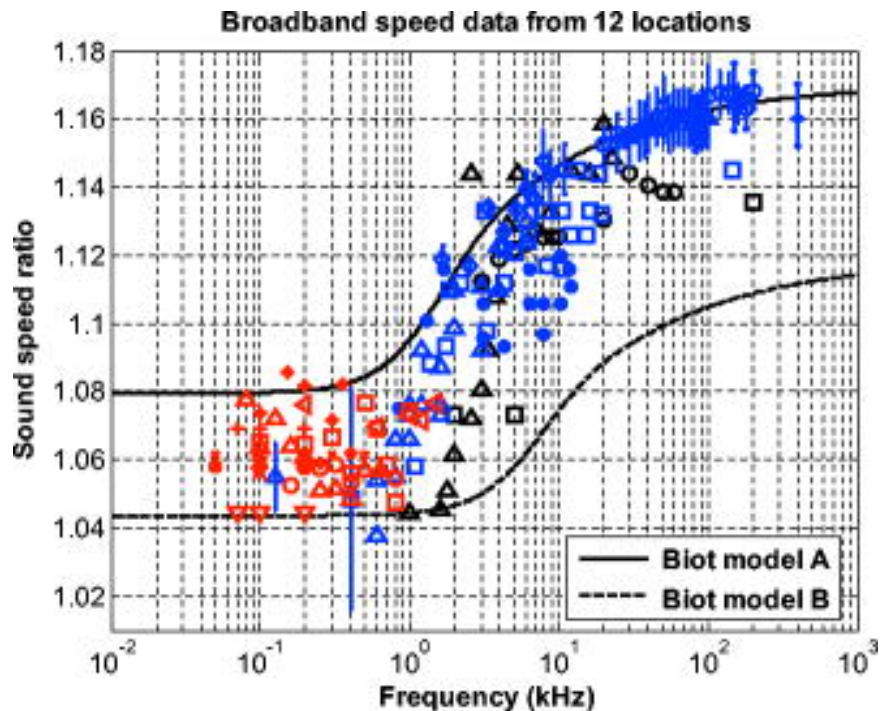


Figure 1.1. Real-World Sound Speed Data vs. Biot Model. Source: [14].

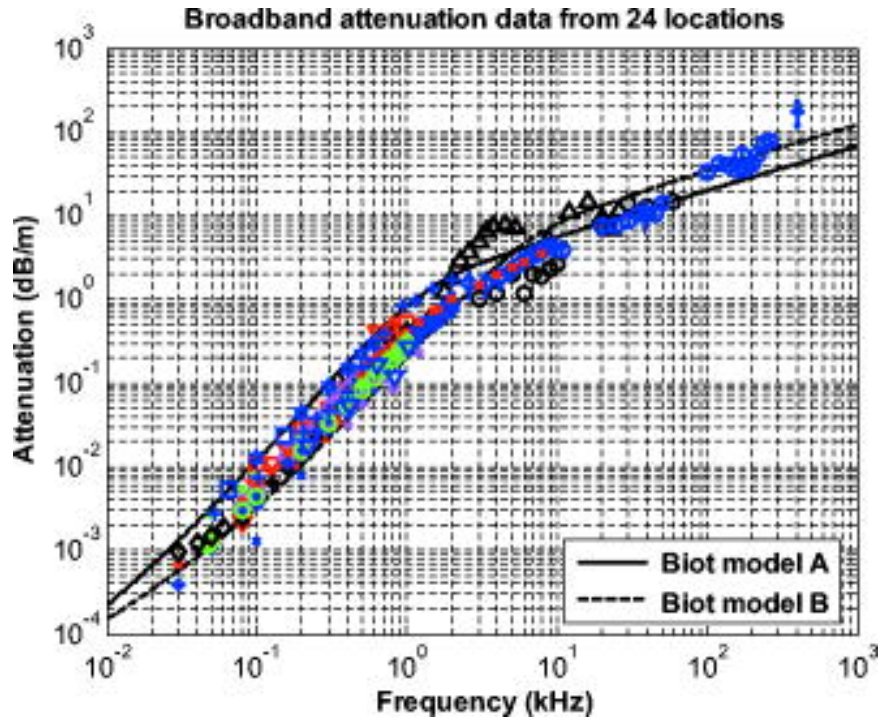


Figure 1.2. Real-World Attenuation Data vs. Biot Model. Source: [14].

Given those definitions we can draw a few conclusions can be drawn from Figures 1.1 and 1.2. Namely, in Figure 1.1 we can see that the sound speed ratio is relatively constant at low frequencies and then begins increasing at some characteristic frequency with an apparent plateau at high frequencies. For the attenuation we can see in Figure 1.2 that two major regions exist with a power law of 2 and $\frac{1}{2}$ relation for low and high frequencies respectively, with the crossover point at a similar frequency for both, between 1 and 10 kHz.

There are several models that attempt to explain the dispersion and attenuation relations present in these two figures. One of the more prominent models has been displayed with the data on these figures using two different sets of fit parameters. The underlying origin of the functions that these data points cluster around is some specific microscopic loss mechanism. Existing models have explored some possible loss mechanisms in an attempt to match to the existing data. The following sections will discuss the features of the existing models.

1.2 Biot-Stoll Model

One major theory in the field was originally developed by M.A. Biot [20]–[22]. Biot originated this theory in the 1950’s hoping to “establish a theory of propagation of elastic waves in a system composed of a porous elastic solid saturated by a viscous fluid” [20]. This original paper focused solely on the low frequency range but was expanded to include the full frequency range in a subsequent paper [21]. Several years later he expanded upon the model to include a "visco-dynamic operator" [22]. This generalized theory was built in a way that focused heavily on the viscosity of the fluid that the sediment was saturated with.

In the 1970s and 1980s this work was expanded upon by Robert Stoll [23]–[26]. Stoll’s work looked to expand the theory originated by Biot and ultimately applied some values to the various fitting parameters to match curves with relatively newer sample sets which can be seen in Figure 1.3.

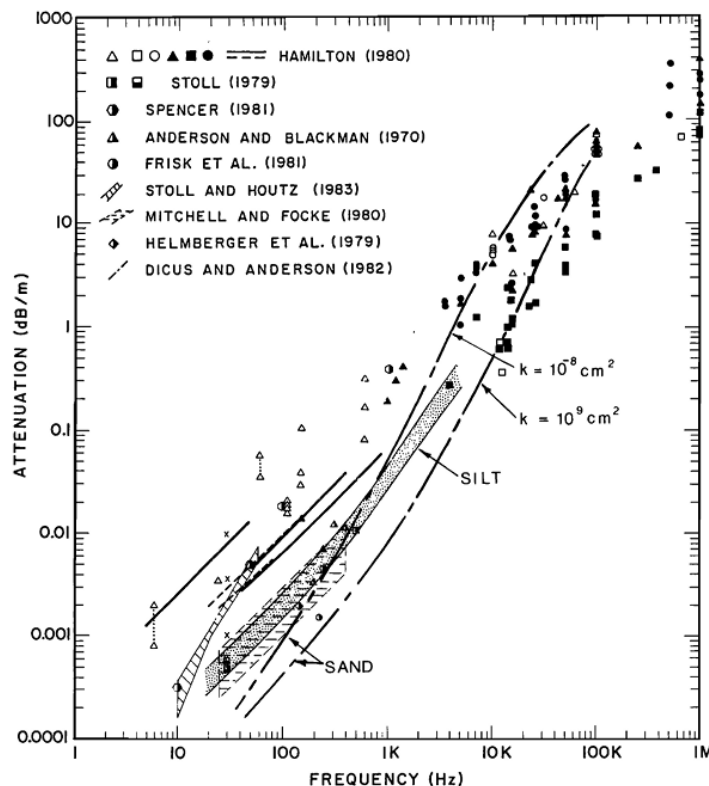


Figure 1.3. Robert Stoll’s Plot of Laboratory and Field Data for Attenuation Dispersion Relation with Biot Theory. Source: [26].

Ultimately the Biot-Stoll theory utilizes a relatively homogeneous makeup for the sediment while focusing on the poro-elasticity of the media and the viscosity of the fluid. This approach requires 13 different fit parameters [27], many of which are difficult, or in some cases impossible, to measure. While Biot's theory was ground breaking and appropriate for porous rocks, and is still widely regarded in the field of ocean acoustics, granular materials are not a poro-elastic frame on which the theory is based. Rather, granular materials are a large collection of discrete objects with inelastic frictional contacts between them. They respond to forces in complex, heterogeneous ways that often make a continuum treatment difficult or impossible. A theory based in the granular nature of marine sediments may be able to simplify our understanding of sediment acoustic properties and provide new insights.

1.3 Buckingham Model

Another widely regarded theory came about in the late 1990s and was motivated by revolutions in the granular mechanics world with regards to force chains. Buckingham [28]–[30] approached the problem with the driving loss mechanism being frictional slips at grain-grain contacts. Buckingham ultimately was able to fit the theory to some data similar to that shown in Figures 1.1 and 1.2 which can be seen in Figure 1.4.

While Buckingham's theory starts from the granular mindset that we want to work from, it still tries to take granular physics and immediately make it into a Partial Differential Equation (PDE), which is an inherently continuum approach [30]. Additionally, the transition between the two power law regimes was only able to be modeled after the effect of viscosity was added [30]. A dry granular material does not exhibit this behavior under the grain-friction model. However, there are many granular phenomena that do not easily lend themselves to a PDE-based approach, as discussed in the following section. Future chapters will discuss that the approach taken here begins by considering the system as a large collection of grains, delaying construction of PDEs or continuum theories. This allows studying these effects directly using particle-based numerical simulations.

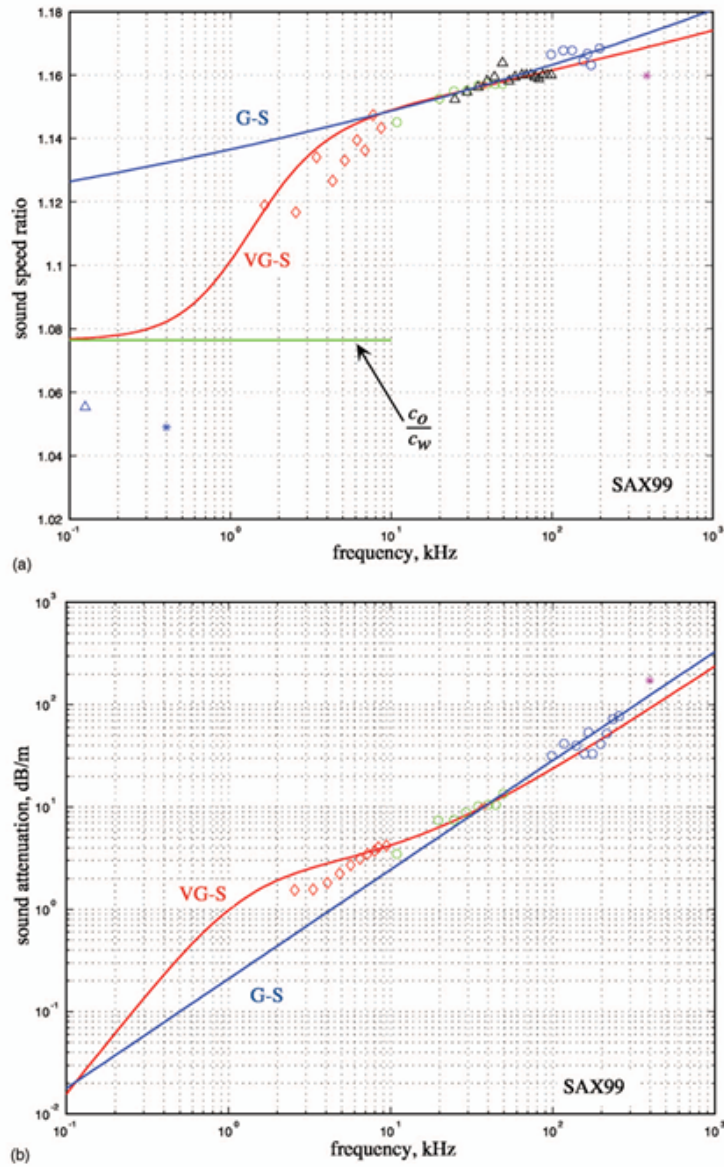


Figure 1.4. Buckingham's VGS and GS Theories Plotted against Select Laboratory Data. Source: [30].

1.4 Sediment Acoustics as a Granular Mechanics Problem

Granular materials exhibit a wide variety of nonlinear phenomena that can be hard to describe or capture with continuum descriptions. These higher dimensional effects will

have a large impact on how these loss mechanisms impact the dispersion and attenuation of the waves propagating through the sediment. In later chapters we will show initial two dimensional results with discussions regarding which of these effects might have impacted the results and in what ways.

Figure 1.5 shows an example of the non-affine motion of grains. Even with a force on the system driving everything linearly left to right, grain movement exists both horizontally and vertically. Rather than grains simply ebbing back and forth from a periodic input, they could bounce around, move up and down, or barely move at all. This motion introduces a higher level of variability to results captured from tracking various grains.

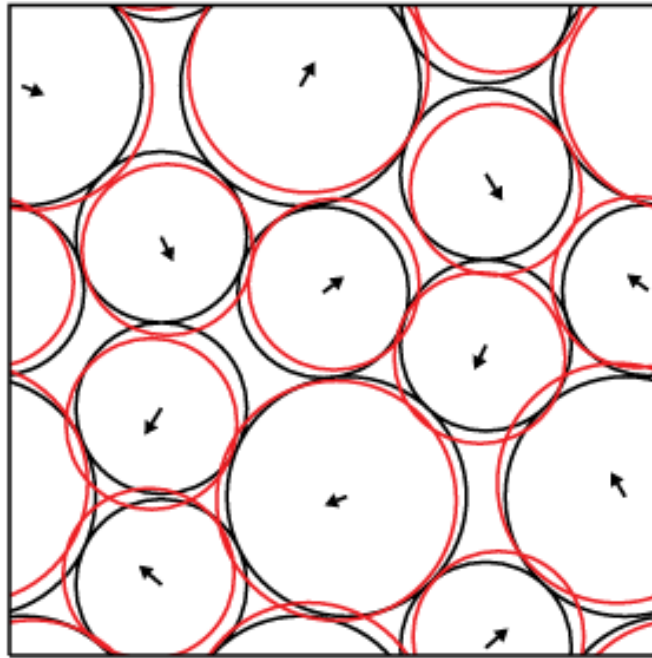


Figure 1.5. Non-Affine Motion of Grains. Source: [31]

Figure 1.6 shows results from a simulation that was impacted by grain-grain contact breaking. In a heterogeneous medium, grains will start with a certain number of contacts, but over time they can shift and no longer maintain contact with the same neighbors. This has impacts on the simulation design and changes the amount of dissipation a certain grain might experience due to a reduction or increase in neighbors.

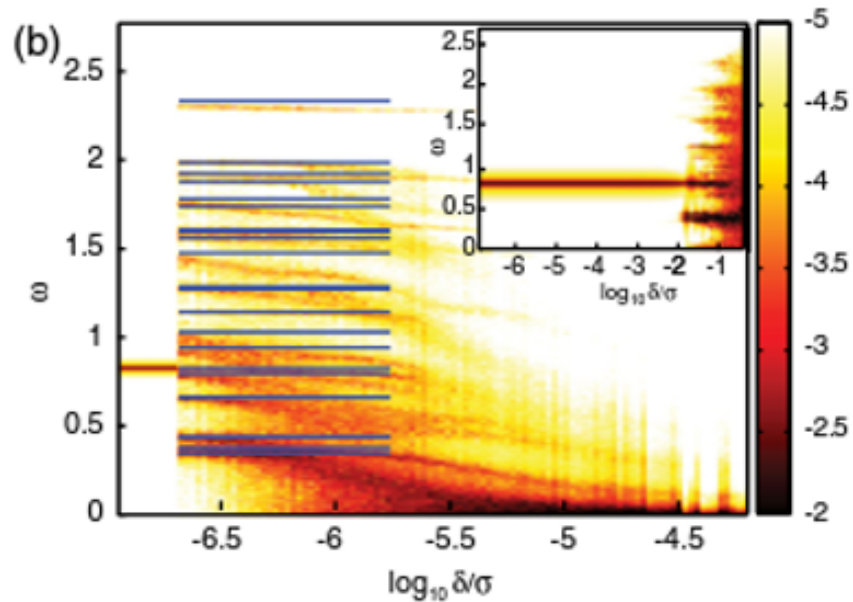


Figure 1.6. Grain-Grain Contact Breaking. Source: [31]

Force chains were a major driving motivation behind Buckingham's theory [28], [29]. An example of these can be seen in Figure 1.7. While the driving force is located at the bottom of this particular image, the forces are propagating through the medium along chains that are highlighted in white. This lends itself to some particles having a large impact on the dispersion of the wave than other and also showcases the nonlinear paths the force is taking through the medium. These force chains can change and move over time as grain-grain contact breaking occurs.

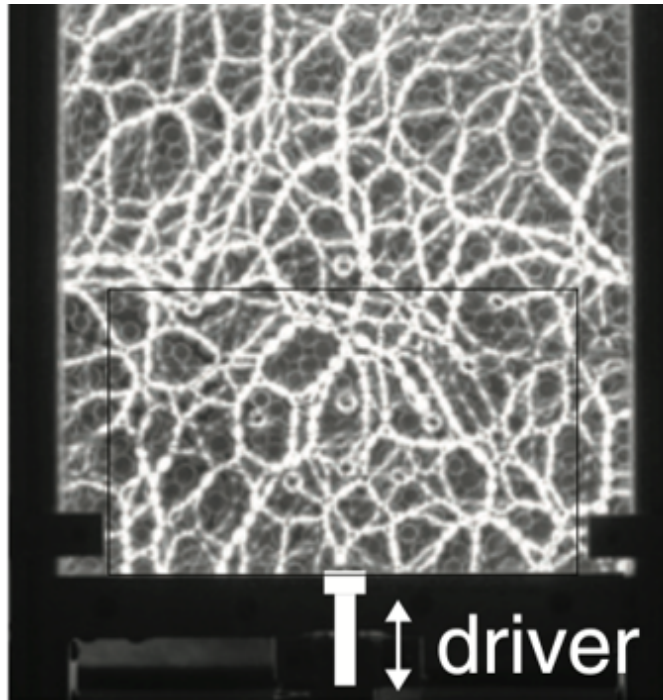


Figure 1.7. Branching of Force Chains. Source: [5]

These effects all contribute to breakdown of basic properties that are commonly assumed in an elastic solid, especially for stiff grain under low pressure. These grains are said to be very near to the jamming or unjamming transition meaning they are close to falling apart [32]. The topic of jamming, a type of glass transition, has been studied intensively over the past two decades, after Buckingham's seminal work was published. Grains typically have just enough contacts to keep the whole system in mechanical stability. Driving such a system excites long-range modes that are often very spatially extended and thus low energy. There are an excess of such modes beyond what is predicted in a typical Debye approach, where the density of modes is assumed to be consistent with plane waves in an elastic solid. Prior work has shown that, for systems at low pressures (relative to the elastic modulus of the grain themselves) that Debye scaling breaks down rapidly [33], [34]. How this and other effects related to the jamming transition influence the acoustic properties of marine sediments has not been fully explored. This thesis represents a first step in that direction.

In this thesis we will model the loss mechanism purely as relative motion between two

grain using a dashpot. This approach is commonly used in simulations of granular media to model inelastic effects at grain-grain contacts, which can be very significant. The numerical magnitude of the dashpot can be directly related to an external physical quantity, typically the restitution coefficient which determines the total energy loss in a grain-grain interaction. This form of energy loss is well established in granular physics but has not been explored as a possible loss mechanism for the acoustic properties of marine sediments. For marine sediments, the dashpot magnitude may be enhanced by the presence of the fluid. In any case, the key idea is to treat the fundamental object as the grains themselves. We will take a grain-focused, discrete-element simulation approach, where all the effects discussed above (e.g., jamming and non-affine motion) are naturally included.

1.5 Conclusion

While existing theories have certain strengths and can be fit to data, a theory based on the granular nature of marine sediments may provide further insights to this problem. The goal of this thesis will be to approach this problem from a strictly granular mindset that focuses on grain-grain forces. In particular, we will consider the system as a collection of inelastic repulsive contacts, where losses at these contacts, in addition to complex motion of grains in 2D and 3D, are responsible for setting the dispersion and attenuation. We show that this approach fits the data over a large range. If successful, this work could drastically simplify our understanding of the acoustic properties of marine sediments.

CHAPTER 2: Theory

The goal of this theory is to approach sediment dispersion as strictly a granular problem. Ultimately, a three dimensional solution is likely to give the best approximation of the real world. While higher dimensional effects are interesting and may be important for a correct description, we first choose to approach the problem in a single dimension to isolate the effect that the grain-grain contact physics has on dispersion. The loss mechanisms utilized will be repulsive contacts between the grains, and a dissipation penalty for relative motion between grains. Common ways to model restitution losses are well established in the discrete element modeling community [35], [36].

2.1 One Dimensional Theory

For this approach we start by trying to answer the question of what are the dynamics of a single chain of grains with dissipating contact interactions? This question is motivated by force chains similar to that seen in Figure 2.1, but rather than having a two dimensional packing of grains we will consider a simplified scenario with a single chain of grains along which forces can propagate.

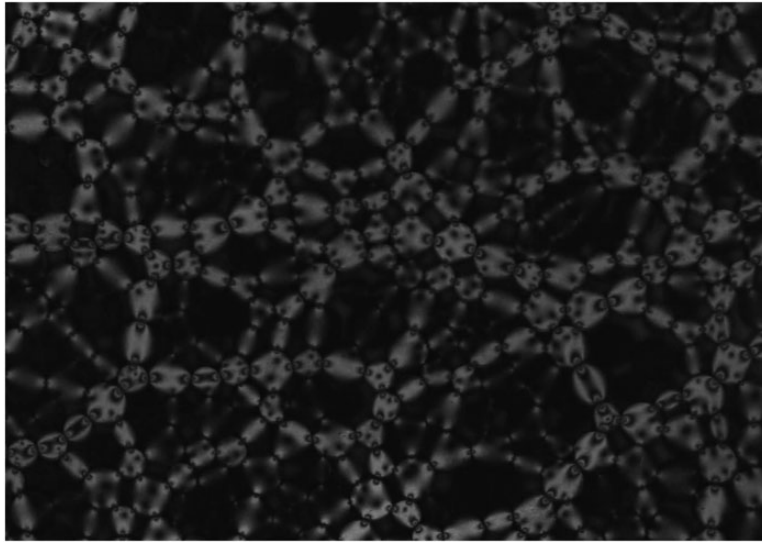


Figure 2.1. Darkfield Photo-Elasticity, Highlighting Force Chains in a Collection of Grains. Source: [37]

Figure 2.2 shows an simplified depiction of this chain of grains. Each grain in the chain is identical in diameter, mass, and material properties. The contacts do not change in one dimension, which reduces the computational complexity as each grain has the same two neighbors at all times. The displacement u_i of grain i from its unperturbed position x on the chain is then governed by the following differential equation, which includes a repulsive spring force and a dashpot for each neighbor $i - 1$ at position $x - d$ and $i + 1$ at position $x + d$:

$$m\ddot{u}_i = \kappa(u_{i-1} - u_i) + \kappa(u_i - u_{i+1}) - \gamma(\dot{u}_{i-1} - \dot{u}_i) - \gamma(\dot{u}_i - \dot{u}_{i+1}). \quad (2.1)$$

Here, m is the grain mass, κ is a spring constant, and γ is the dashpot coefficient, while dots denote time derivatives. From this starting point, using the limit definition of a derivative and assuming d is small (i.e., the long-wavelength limit), the following wave equation emerges

$$mu_{tt} = \kappa_n d^2 u_{xx} + \gamma_n d^2 u_{txx}, \quad (2.2)$$

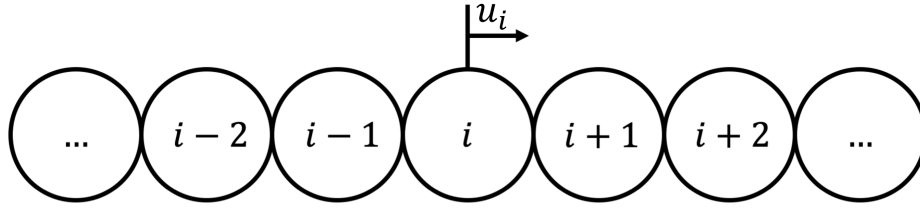


Figure 2.2. One Dimensional Chain of Identical Grains

where subscripts t and x now denote derivatives with respect to time and space, respectively. Guessing a decaying plane wave given by

$$u(x, t) = Ae^{-\alpha x} e^{i(kx - \omega t)}, \quad (2.3)$$

we can then solve the system to arrive at the two following equations:

$$\hat{\alpha} = \hat{\omega}^2 \frac{\hat{\gamma}}{\sqrt{2}} \left\{ [1 + (\hat{\omega}\hat{\gamma})^2] \left[1 + \sqrt{1 + (\hat{\omega}\hat{\gamma})^2} \right] \right\}^{-1/2} \quad (2.4)$$

$$\hat{k} = \hat{\omega} \frac{1}{\sqrt{2}} \frac{\left\{ [1 + (\hat{\omega}\hat{\gamma})^2] \left[1 + \sqrt{1 + (\hat{\omega}\hat{\gamma})^2} \right] \right\}^{1/2}}{1 + (\hat{\omega}\hat{\gamma})^2}, \quad (2.5)$$

The dimensionless quantities in Eqs. (2.4) and (2.5) are defined by the following equations:

$$\hat{k} = kd \quad (2.6)$$

$$\hat{\alpha} = \alpha d \quad (2.7)$$

$$\hat{\omega} = \omega \sqrt{m/\kappa} \quad (2.8)$$

$$\hat{\gamma} = \gamma / \sqrt{\kappa m}. \quad (2.9)$$

the wavenumber and attenuation coefficient each have dimensions of inverse meters, and are easily nondimensionalized by the grain diameter. Angular frequency is non-dimensionalized

by the resonance angular frequency, and the dashpot term is non-dimensionalized using the ratio of the energy lost and energy stored per cycle, which is related to the Q factor of the contact [38].

The functional forms presented in (2.4) and (2.5) give us the relationships similar to those discussed in 1. Particularly, this gives us attenuation proportional to frequency squared and frequency to the one-half power at low and high frequencies respectively. For wave speed, the result is constant at low frequencies and then increases at higher frequencies. This solution does not taper and subsequently level off like the real world data in Figure 1.1. However, this solution is based on an incredibly idealized situation that may not be representative of the real world. As we will see later, certain higher order effects that present themselves in multiple dimension may account for high-frequency asymptotic behavior of the wave speed.

It is interesting to compare these solutions to the mathematical form of those for classic viscosity [39]. While there is a mathematical similarity, these equations have crossover points which are set by the granular behavior that has been defined above vice the viscosity of the fluid in which the wave is propagating.

Another key accomplishment of these two equations is that we now have just one fit parameter, that being the value of the dash-pot as specified by $\hat{\gamma}$. Picking the value of the dash-pot and guessing real world values we can plot the data pulled from Figures 1.1 and 1.2. As we can see in Figures 2.3 and 2.4, the curves closely approximate the real world data with the exception of the taper at higher frequencies for speed.

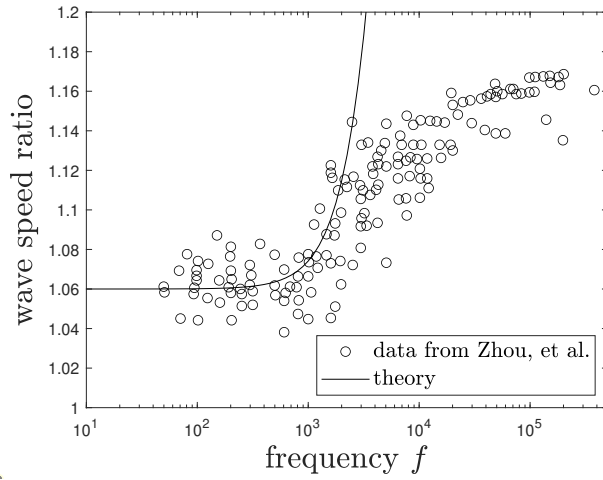


Figure 2.3. Real World Speed Data vs. 1D Theory

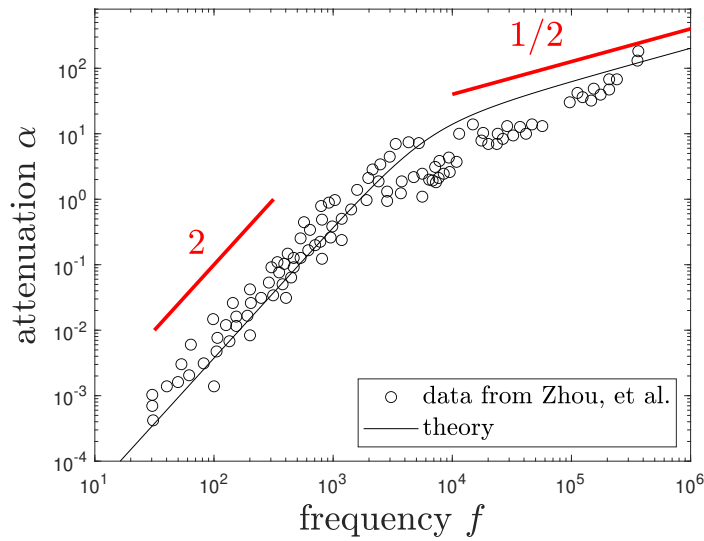


Figure 2.4. Real World Attenuation Data vs. 1D Theory

2.2 Connecting to Physical Parameters

A key question for the grain-focused approach relates to its ability to correctly predict the frequency dependence of attenuation and phase speed. Of particular importance is connecting physical parameters like grain size, stiffness, and mass density with the crossover frequency f^* at which the data show that the phase speed begins to increase and the frequency dependence of the attenuation coefficient changes. The theory discussed above clearly show that f^* corresponds to the case when $\hat{\omega}\hat{\gamma} = 2\pi f\gamma/\kappa \approx 1$. Thus, $f^* \approx \kappa/2\pi\gamma$. The data from Figures 1.1 and 1.2 suggest a value of f^* between 1 and 10 kHz. In Table 2.1, we consider two cases where parameters are chosen based on different physical reasoning, as explained below.

Table 2.1. Parameter Values

Parameter Values					
Case	κ (N/m)	γ (N·s/m)	d (mm)	ρ (kg/m ³)	f^* (kHz)
Case 1	5×10^3	0.1	0.1	2500	8
Case 2	3.3×10^5	10	0.1	1900	5.2

In the first case, we consider a purely granular situation. Hertzian contact mechanics states that the force between two particles of the same elastic modulus E but possibly differing radius $R = d/2$ is not a linear spring but instead a nonlinear spring, with force law

$$F = \frac{4}{3}E^*R_{\text{eff}}^{1/2}\delta^{3/2}$$

Here, $E^* = E/2(1 - \nu^2) \approx E/2$ if $\nu \sim 0.25$ or smaller and $R_{\text{eff}} = 1/(1/R_1 + 1/R_2) \approx R/2$ if $R_1 \approx R_2 \approx R$. Thus,

$$\kappa \equiv \left. \frac{dF}{d\delta} \right|_{\delta_0} = E\sqrt{\frac{R\delta_0}{2}}$$

The value of δ_0 is set by the confining pressure, $P_0 = F_0/d^2 = F_0/4R^2$. This yields:

$$4R^2P_0 = \frac{2}{3}E\sqrt{\frac{R}{2}}\delta_0^{3/2}.$$

Solving this equation for δ_0 gives

$$\delta_0 = \left(6\sqrt{2}\sqrt{P_0/E}\right)^{2/3}$$

, and

$$\kappa \approx 0.72Ed \left(\frac{P_0}{E}\right)^{1/3} \quad (2.10)$$

For sediment, $E \approx 50$ GPa (5×10^{10}), $d \approx 0.1$ mm (10^{-4}), $P_0 \approx (\rho_s - \rho_l)gh$, where $\rho_s \approx 2500$ and $\rho_l \approx 1000$ are the mass densities of the sediment and liquid, respectively, $g \approx 9.8$ is the gravitational acceleration and h is the depth of the sediment in question. If we assume $\Delta\rho \approx 1500$ and $h \approx 10$ cm, then $P_0 \approx 150$ Pa. Plugging these values in gives:

$$\kappa \approx 5 \times 10^{10} \times 10^{-4} \left(\frac{10^2}{5 \times 10^{10}}\right)^{1/3} \approx 6 \times 10^3 \text{ N/m}$$

We note that even increasing the depth by an order of magnitude, raising P_0 by an order of magnitude, only increases κ by a factor of 2. Thus, value of κ is only weakly dependent on h via $h^{1/3}$. Additionally, note that $\kappa \approx 6 \times 10^3$ N/m is considerably smaller than what would be estimated from simple dimensional analysis, $\kappa \approx Ed \approx 5 \times 10^6$ N/m. This follows directly from Hertzian contact mechanics. The predicted wave speed from dimensional analysis at low frequencies would be $c_0 \approx d\sqrt{\kappa/m} \approx 200$ m/s, which is smaller than the typically observed wave speeds by nearly an order of magnitude. Thus, we conclude that a purely granular model, neglecting the fluid altogether, will likely be incomplete. However, using this reasoning, a value of $\gamma \approx 0.1$ N·s/m would yield $f^* \approx 8$ kHz, which is within the range of acceptable f^* from Figures 1.1 and 1.2. The physical justification for this value of γ would require further consideration.

In the second case, we consider that the low-frequency phase speed is known as approximately 1600 m/s, according to the low-frequency data in Figure 1.1. In this case, $\kappa \approx m(c_0/d)^2 \approx 3.3 \times 10^5$. In this situation, the effective stiffness of the material arises not primarily from grain-grain contact interactions but from a hybrid granular-fluid matrix. Further work is needed to interpret this picture. We take d to be the grain size,

and ρ could either be from the grains, $\rho \approx 2500 \text{ kg/m}^3$, or from a hybrid of grains and fluid, $\rho \approx \phi\rho_s + (1 - \phi)\rho_l \approx 1900 \text{ kg/m}^3$. This would yield an effective mass of $m \approx \frac{\pi}{6}\rho d^3 \approx 1 \times 10^{-9} \text{ kg}$. A value of $\gamma \approx 10$ would yield $f^* \approx 5 \text{ kHz}$. Again, whether this value of γ is physically reasonable remains a question for future study.

2.3 Conclusion

We now have theoretical equations (Eq. (2.5) and (2.4)) for the wave speed ratio and the attenuation as a function of the wave's frequency with one simple fit parameter in the dash-pot value $\hat{\gamma}$. Once these are validated we can move into higher dimensions and begin to evaluate the differences and effects in those realms.

CHAPTER 3: Simulation Methodology

In order to confirm the model, (Eqs. 2.4 and 2.5) while simultaneously developing an analysis tool-set, we built and ran one dimensional simulations. Both the simulations themselves, and the analysis tool-set were designed in a way that they could serve as the frame work for future simulations in higher dimensions. Simulations were constructed in MATLAB to be run on the Hamming Cluster Computer at the **NPS!** (**NPS!**). Utilization of cluster computing allowed for simultaneous generation of dozens of data sets with each iteration of the simulation.

Upon completion of the 1D simulation validation, simulations were built in two dimensions. The following sections will outline initial conditions, driving mechanisms, and time-domain integration schemes for each simulation while highlighting any differences that exist between the one and two dimensional simulations.

3.1 Inputs and Setup

While a large number of similarities exist, there are some major differences in the set up for the one dimension and two dimension simulations that will be outline in the following sections.

3.1.1 One Dimension Simulation Setup

The simulation software allows for the input of all parameters of the 1D chain of grains. The number of grains to be used N , the mass of each grain M , and the spring constant κ are inputs. While the ability to adjust the diameter of the grains was considered, it was ultimately left fixed at 1 across all simulations, since the non-dimensional parameters should take this into account. An array of the initial positions is created with the grains evenly spaced so they are exactly 1 grain diameter apart. These initial positions are then reduced by 10% to create for an initial overlap in the system. Figure 3.1 shows what a small chain of grains would look like upon set up.

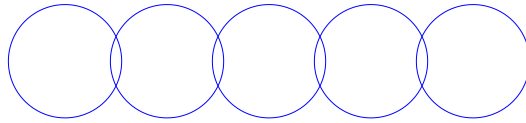


Figure 3.1. Small One Dimensional Chain of Grains

Lastly the driving frequency ω and dash-pot value γ are input into the simulation. These two parameters will be varied heavily to attempt to reproduce the curves created by Equations 2.4 and 2.5. Additionally, the driving frequency is used to determine the size of each time step in the simulation according to:

$$dt = 0.002 \frac{2\pi}{\sqrt{\frac{\kappa}{M} - \left(\frac{\gamma}{2M}\right)^2}}, \quad (3.1)$$

which is 0.002 times the natural period of damped oscillations of each grain-grain contact. Having defined the simulation parameters, we now generate and zero vectors for the horizontal velocity and acceleration of each grain.

3.1.2 Two Dimension Simulation Setup

A major goal of the two dimension simulations was to begin to evaluate the impacts of some of the higher order effects that were previously discussed. For this reason the initial conditions for the grains couldn't be generated as a homogeneous array of identical grains. Rather, a random packing of a mix of different grains needed to be created and compressed into a box with a certain initial system pressure.

We begin by making a large box, the dimensions of which are based on the number of grains, the grain diameter and a user defined width factor W_{factor} . This box has rigid horizontal boundaries and periodic upper and lower boundaries. The initial dimensions of the box (L_x and L_y) are set using the following equations.

$$L_x = \frac{ND}{W_{\text{factor}}} \quad (3.2)$$

$$L_y = \frac{ND}{2} \quad (3.3)$$

The grains themselves can not all be one diameter or we would eventually just end up with a pressurized grid of identical grains. Without a disordered medium we would essentially be stacking several identical iteration of the one dimensional simulation on top of each other. This would not result in the higher dimensional effects discussed previously. Currently we are introducing heterogeneity by utilizing two grain diameters. A factor for the second grain diameter is input by the user and half of the grains are given this diameter. To randomize the grain diameter, MATLAB's `rng()` function is seeded with a user input seed, and then the `rand()` function is used to randomize which grains are members of the set of larger or smaller diameters. Upon completing this grains are assigned an initial x and y coordinate using MATLAB's `grid()` function.

Now having a large box with grains distributed throughout it, the box needs to be shrunk so that the grains are pushed together and the system pressurized. The simulation integration scheme that is discussed in the following section is then utilized as the upper periodic boundary is lowered. Every time step the potential energy, E_p , and the kinetic energy, E_k , per grain are determined using

$$E_p = \frac{1}{N} \sum \frac{1}{2} \kappa \left(\frac{D_n - D_{n-1}}{2} - r \right)^2 \quad (3.4)$$

for the potential energy, and

$$E_k = \frac{1}{N} \sum \frac{1}{2} M v_n^2. \quad (3.5)$$

for the kinetic energy. With M being the grain mass, v_n being a particular grain's velocity, D_n being a grain's diameter, and r being the distance between two grain centers. The potential energy is then used to calculate the pressure for each time step using

$$P = \sqrt{\frac{2E_p}{\kappa}}. \quad (3.6)$$

A binary search method is utilized to determine the final position of the upper periodic boundary. Until the pressure is greater than 2% of the target pressure, the upper periodic boundary and all particles are lowered by 1% of their current y value. Once this condition is no longer met but the system pressure is still less than the target pressure and the kinetic energy is lower than 1×10^{-8} this same method is still applied. Once the pressure is larger than the target pressure the upper boundary will stop moving until kinetic energy has reduced to less than 1×10^{-10} . At this point, the upper boundary will raise by 1% of its current height and allow the system to slightly depressurize.

The system will now begin the same process but with variations of the upper boundary and grain vertical positions now being at a factor of the target pressure. Once the system reaches a point where the pressure is greater than the target pressure and the kinetic energy is less than 1×10^{-20} , the packing is considered complete and the initial condition is saved.

Ultimately most simulations used a packing with 10,000 grains at diameters of 1 and 1.4 with a width factor of 10 (channel is 1000 units long). A wide variety of different packing target pressures were used with seed numbers ranging from 1-5. An example of a packing pressurized to 0.1 can be seen in Figure 3.2 while an example of a system pressurized to 0.01 can be seen in Figure 3.3.

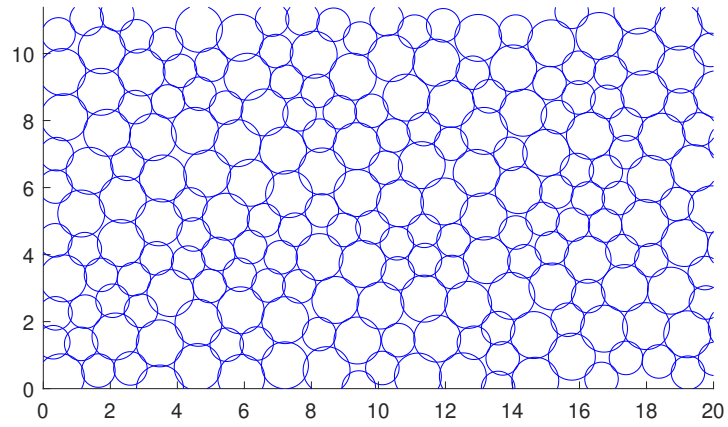


Figure 3.2. Over Pressurized Packing of Grains in Two Dimensions

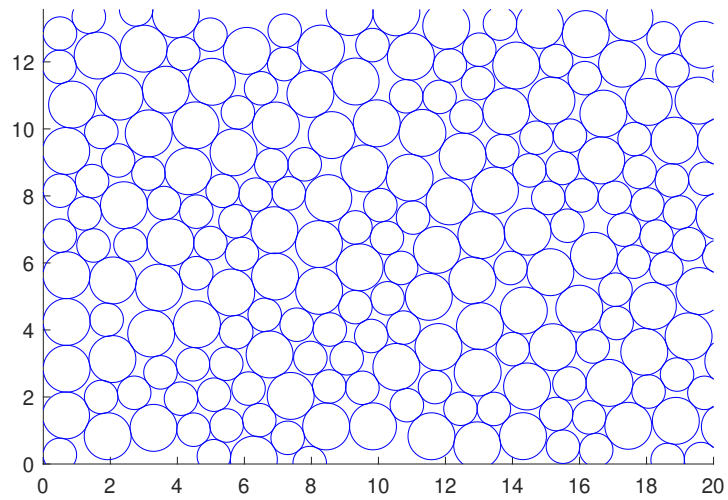


Figure 3.3. Under Pressurized Packing of Grains in Two Dimensions

3.2 Simulation Integration Scheme

The simulation numerically steps through the force equation for each grain using a velocity Verlet integration scheme [40]. The implementation of this in one dimension will be discussed first followed by an explanation of differences that exist for the two dimensional simulation.

3.2.1 One Dimension Integration Scheme

In one dimension we have a known neighbor list for grains. Every grain is neighbored by the $i+1$ and $i-1$ grains and no others. This drastically simplifies the calculation of forces on each grain. The position of each grain is updated every integration step according to:

$$x_n(t_i) = x_n(t_{i-1}) + v_n(t_{i-1})dt + \frac{1}{2}a_n(t_{i-1})dt^2 \quad (3.7)$$

where n denotes the grain number in the chain, and i denotes the current time step. After each particle's position is updated, the force acting on grain n due to neighboring grain m is calculated using:

$$F_{nm} = \kappa[D_{nm} - (x_n - x_m)] - \gamma(v_n - v_m) \quad (3.8)$$

where D_{nm} is the average grain diameter of grains n and m defined by:

$$D_{nm} = \frac{d_n + d_m}{2}. \quad (3.9)$$

The acceleration of each grain is then determined by dividing the sum over m of forces F_{nm} by the mass M . Last, the velocity is updated according to:

$$v_n(t_i) = v_n(t_{i-1}) + \frac{a_n(t_{i-1}) + a_n(t_i)}{2}dt \quad (3.10)$$

where once again n denotes the grain number in the chain and i denotes the current time step. With the velocity and acceleration for the current time step calculated, all inputs for

Equation 3.7 for the following time step have been determined.

3.2.2 Two Dimension Integration Scheme

The biggest challenge in two dimensions is the implementation of a neighbor list. Unlike the one dimension model described above, we can not readily assume that a given grain will have a set number of contacts or that they will remain constant throughout the course of the simulation. The simulation uses a fixed neighbor list, where neighbors are determined at the beginning of the simulation and held constant throughout. At this point only low amplitudes are being used for the driving force so this it is assumed there will be little to no contact breaking.

The neighbor list is developed by going through every grain and determining how many other grains are touching or overlapping from the initial condition set. While the simulation is running every grain, n , is compared to every one of its neighbors, m . Typically grains have anywhere between 4 and 8 neighbors. The force vector acting on grain, n , is then calculated by summing the force vectors from each neighbor, m , that are calculated using

$$\vec{F}_{nm} = \kappa(D_{nm} - |\vec{r}_n - \vec{r}_m|)\hat{n}_{nm} - \gamma[(\vec{v}_n - \vec{v}_m) \cdot \hat{n}_{nm}]\hat{n}_{nm} \quad (3.11)$$

with \hat{n}_{nm} being the normal vector between grains n and m . The acceleration, velocity, and displacement for each grain, n , is updated using the same method described in the previous section but with x and y components vice just x.

3.3 Simulation Driving

The acoustic waveform must now be input into the simulation or else we will simply have a static line of overlapping grains. Driving of the simulation was accomplished by specifying the displacement of the first grain in the 1D system, and by a line of particles in the 2D system. In addition to the position of the first grain being forced, the last grain was held stationary throughout the entirety of the simulation. Two methods of driving the simulation were ultimately utilized as different frequency ranges presented different challenges in measuring the attenuation and the wave speed. The vast majority of the data was taken using a pulsed input, while some higher frequency modes required a continuously driven

input with a constant amplitude. Each input method was implemented by directly updating the position of the first particle each time step.

3.3.1 Continuous Driving

Initially the simulation was developed to drive the first grain at a constant amplitude and frequency. Every time step the simulation would update the first grain's position according to:

$$x_1(t_i) = x_1(t_0) + A \sin(\omega t_i) \quad (3.12)$$

where $x_1(t_0)$ is the grain's position at the beginning of the simulations and A is the amplitude of the driving. This method ultimately produced wave forms such as what we see in Figure 3.4.

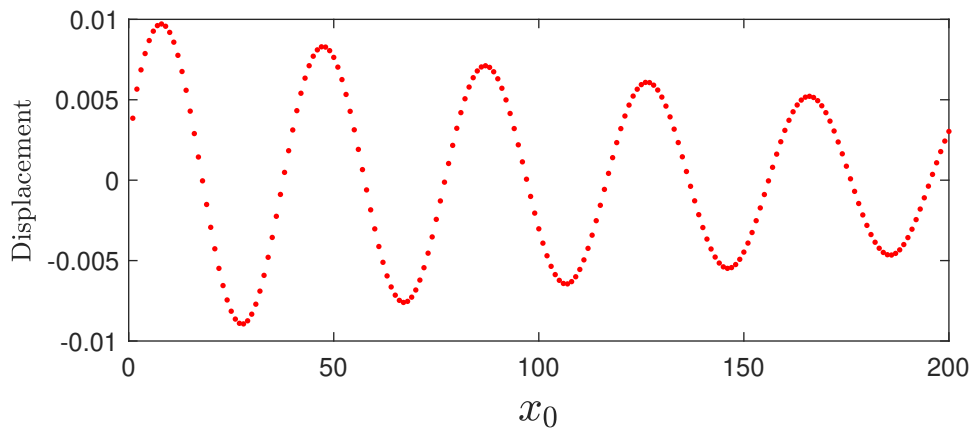


Figure 3.4. Plot of Grain Displacement for Continuously Driven Chain of Grains

This driven method was the initial approach but had one major flaw. The abrupt movement of the first particle at the beginning of the simulation led to a shock that would propagate along the chain with little dissipation. This affected initial data processing attempts, and led to the development of the pulsed driving mechanism that will be discussed next. However, this driving mechanism ultimately proved useful for simulations with higher driving frequency

and higher dissipation (which attenuated the initial shock), and the data extraction methods utilized for those will be discussed as well.

Two Dimension Continuous Driving

Ultimately the two dimension simulations are continuously driven. This is accomplished by moving all grains contacting the left wall of the simulation similar to Eq. (3.12).

3.3.2 Gaussian Pulse

A second type of driving was developed by applying a Gaussian envelope shape to the driving sinusoid. . This method minimizes the infinite-frequency content inherent at the first instant of driving at the cost of including a small spread in frequencies. It also serves as a confirmation of our measurements in the constant driving case. The Gaussian envelope was implemented by using the following update to the displacement of the first particle,

$$x_1(t_i) = x_1(t_0) + A \sin(\omega t_i) e^{-(t-t_{\max})^2/\sigma} \quad (3.13)$$

where $\sigma = \tau/\sqrt{2 \log 2}$ is the pulse width, and is related to the half power full width of the pulse, τ . The parameter t_{\max} controls the starting time of the pulse relative to the peak, and sets the truncation of the Gaussian function, since it has infinite support. This parameter was set to 4τ , and the pulse length, τ was set to five cycles.

This equations relied solely on the value of the driving frequency ω to determine the function for the envelope. Figure 3.5 shows an example of a pulsed waveform. Each color represents the pulse at a different time in the simulation. Additionally, the green line shows the tracked peak location of the pulse as it propagates along the particle chain. This peak position is important for data processing that occurs upon completion of the simulation.

3.4 Conclusion

Having developed a simulation models for one and two dimensions we now need to develop the tool set to extract and analyze the data. A large number of data sets were able to be run with all parameters of mass, driving frequency, spring constant and and dash pot value

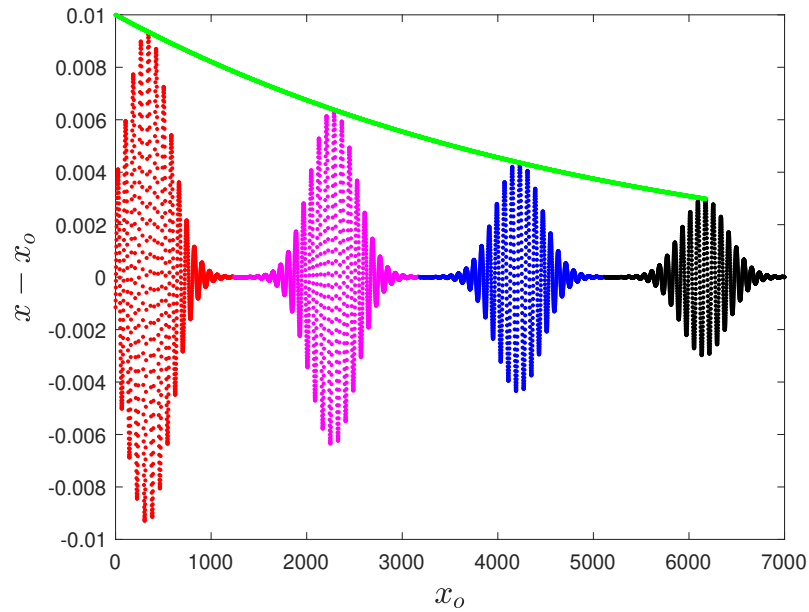


Figure 3.5. Snapshots of Gaussian Pulsed Waveform Displacement at Four different times with Peak Tracking.

being varied. Additionally for the two dimension simulations, each collection of variables was run using a variety of initial conditions with various seeds and pressures. The next chapter will discuss how the analysis tool sets for each simulation type are developed and the results that have been achieved thus far.

CHAPTER 4: Data Processing and Results

While use of the Hamming Cluster Computer allows for multiple simulations to be run rapidly and simultaneously, the post processing of the data was completed separately. This required simulation results to be packaged with all meaningful information to determine the attenuation and dispersion for any given data set. This chapter will discuss the data extraction methods used for the one dimension simulations followed by their results. From there the changes necessary for two dimension data extraction will be discussed along with preliminary results for two dimension simulations.

4.1 One Dimension Data Extraction

4.1.1 Attenuation

Ultimately determining the attenuation was a straight forward task. With each wave expected to follow Equation (2.3), we simply needed to track the peak amplitude reached for each grain throughout the life of the simulation. Figure 4.1 shows a log plot of the peak positions that was tracked throughout the simulation shown in Figure 3.5. The red points denote the grains that pulse reached, and the blue points denote those that weren't reached by the simulation. A linear fit semi-log space is applied to the red grains to get the decay parameter $-\alpha$ for this particle data set.

4.1.2 Wave Speed

The wave speed proved more difficult than the attenuation to determine. For simulations with high ω and high γ the wave would decay in tens of grains vice hundreds or thousands of grains. For this reason two different methods were applied based on the type of input used.

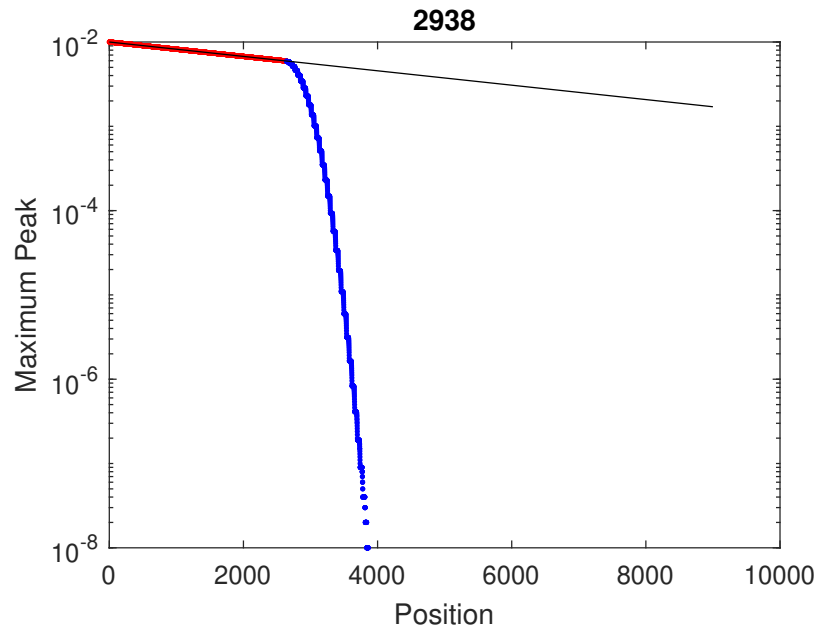


Figure 4.1. Log Plot of Peak Positions Tracked Through Simulation

Pulsed Input

The primary method of extracting wave speed from the data was to track the time step at which the peak position was recorded for each grain. This time step could then be used to determine the amount of simulation time it took for the wave peak to travel from the first grain to any given particle in the chain. Dividing the position of any given grain in the chain by the time it took the wave to get there we get a value for speed. The speed was then determined by taking the average of these values for the middle half of particles over which data was collected. This allowed us to filter out any noise that existed at the beginning or end of the chain. While consistent and stable results were easy to obtain for low ω and/or low γ simulations, the data was often too noisy when the simulation had high values for γ and ω . Similarly to the section above, Figure 4.2 shows a plot of the data extracted from the simulation in Figure 3.5 with the line representing the determined speed.

Continuous Input

Given that waves with high ω and high γ were decaying in the tens of particles a different approach was needed to determine wave speed for these parameter sets. The continuously

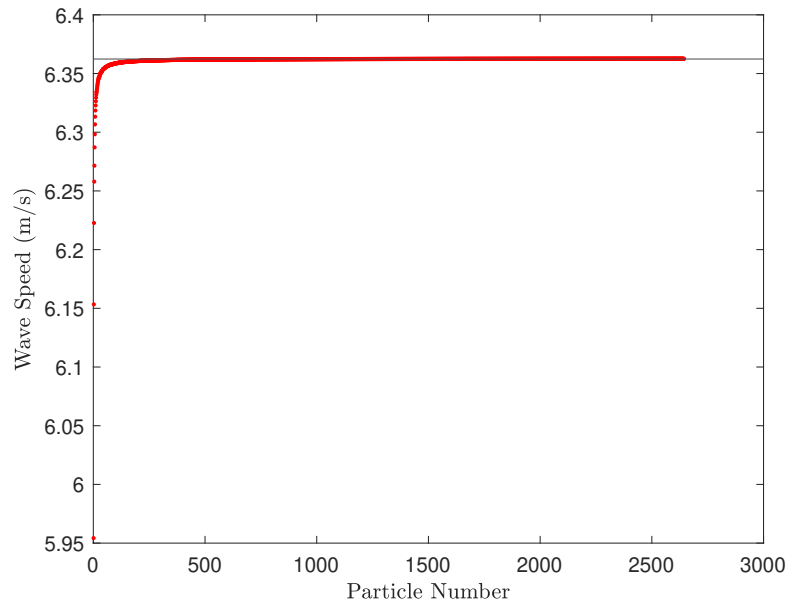


Figure 4.2. Calculated Wave Speed vs. Particle Number for Gaussian Pulsed Simulation

driven input was used with the position of each particle saved for every time step in the simulation. A sinusoidal waveform was then fit to each data point using Equation (4.1).

$$A \sin(\omega t + \phi) + C \quad (4.1)$$

The amplitude, A , for each fit could also be used to determine the attenuation coefficient for these data sets, but ultimately this approach was not used as that data was achievable from the pulsed simulations. Figures 4.3 shows an example of two particles in one simulation with the fit for each particle. Note the difference in amplitudes between the two particles.

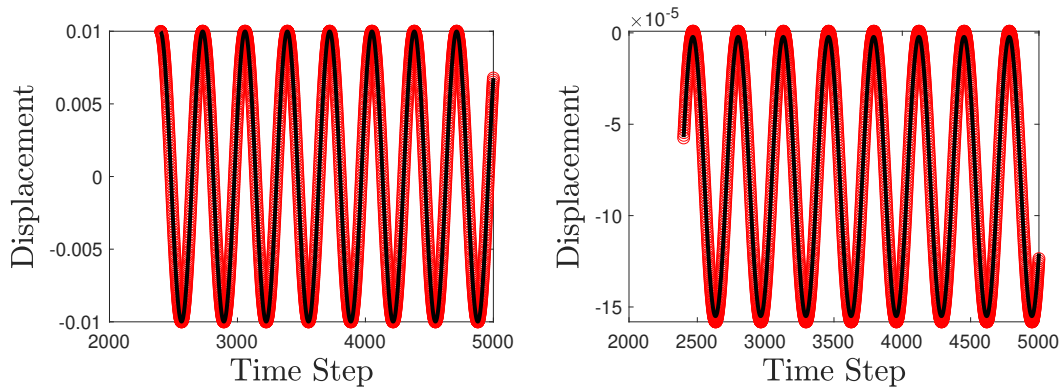


Figure 4.3. Particle Displacement vs. Time for Two Particles in Same Simulation

The phase difference between each particle and the following particle was then determined. The average of these differences was utilized to the wave number and subsequently from that the wave speed for that given data set using Equations (4.2) and (4.3).

$$k = \frac{\Delta\phi}{D} \quad (4.2)$$

$$c = \frac{\omega}{k} \quad (4.3)$$

Where c denotes the wave speed obtained, $\Delta\phi$ denotes the phase difference, and D denotes the distance between two particle centers (in the case of all simulations this was 0.9).

4.2 One Dimensional Results

Having developed methods to simulate and analyze waves propagating along the linear chain of grains we now seek to validate that the simulations match the theory that was derived in Chapter 2. This will allow us to see that the simulations are working as expected and that the data extraction methods will work for higher dimensions.

Figures 4.4 and 4.5 show the results of the 1D simulations for attenuation and speed

respectively. The black lines denote the theory presented in Equations (2.4) and (2.5) respectively. The various symbols and color gradient scale denote different levels of $\hat{\gamma}$. The x-axis for each graph is $\hat{\omega}\hat{\gamma}$. All values have been non-dimensionalized by the equations listed in Chapter 2.

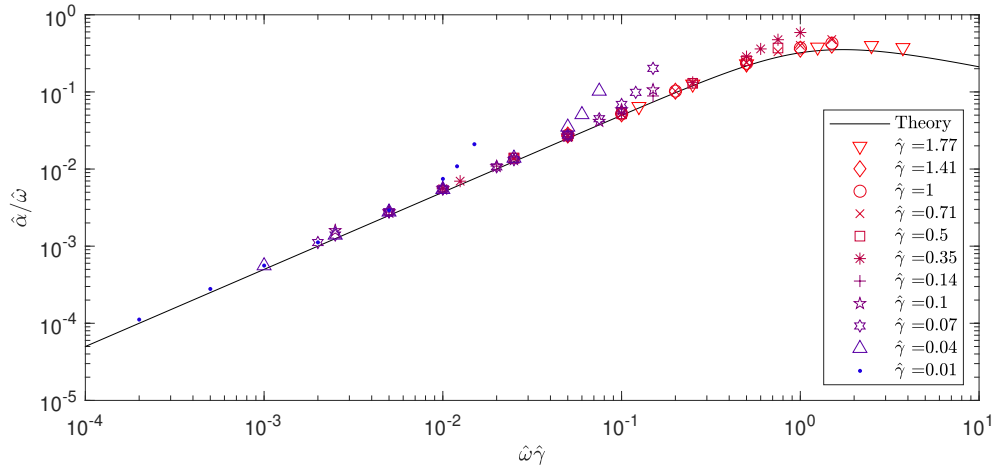


Figure 4.4. Attenuation Results vs. Theory for 1 Dimension Simulations

For the most part the results are consistent with the theory. We do see a slight dip below the constant wave speed in the final decade before the theory predicts an increase, and all values after that fall slightly below the theory. Additionally nearly all of the attenuation predictions are higher values than predicted.

4.3 Two Dimension Data Extraction

Many similarities to the data extraction method for continuous driving for one dimension exist as we shift to two dimensions. For this, every particle's x position is stored every time step of the simulation. Upon completion, Eqn. (4.1) is fit to each particle's simulation waveform. This provides us with an amplitude A , a phase ϕ , and the initial position x_0 for each particle. From there, attenuation is handled the same as above with a linear fit of the logarithm of the amplitudes vs initial particle position data. The phase data is now handled much the same way, with a linear fit being applied to the phase vs particle initial position data. The slope of this fit is the wave number k which is used to calculate the wave speed using Eqn. (4.3).

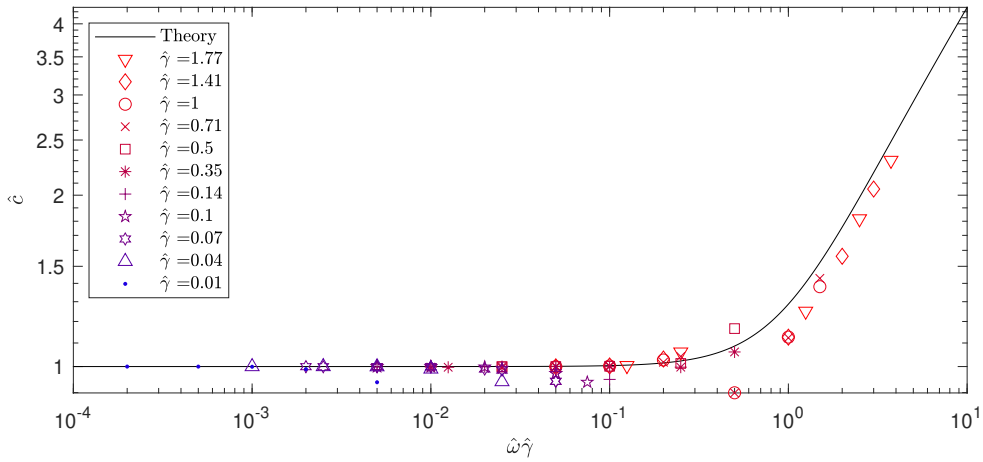


Figure 4.5. Wave Speed Results vs. Theory for 1 Dimension Simulations

4.4 Two Dimension Results

Having developed the tools to extract the final data from the two dimension simulations the results can now be plotted. However, a large difference exists from the results for the one dimension simulations as the initial conditions are varied for the two dimension simulations. For every initial pressure that was used, 5 different seed values were used to randomize the particle diameters. Before getting into the attenuation and dispersion results we will first take a look at snapshots of a simulation run on two initial conditions with different initial pressures.

Figure 4.6 displays a snapshot of particle displacements for given point in time. This simulation was run on the initial condition shown in Figure 3.2. Each red dot represents a particle, with the x axis being the particle's initial horizontal position, x_0 , and the y axis representing the particles horizontal displacement at this point in time. Give the amount of initial overlap between particles and the low amplitude of the driving force, we can see that the wave propagates through in a very orderly manner.

Next we look at a system that has a lower pressurization like that seen in Figure 3.3. The snapshot for this simulation is shown in Figure 4.7. Once again the data is presented in the same format. With the exception of the target pressure for the initial condition all other values were held constant between these two figures. While it is still possible to trace the

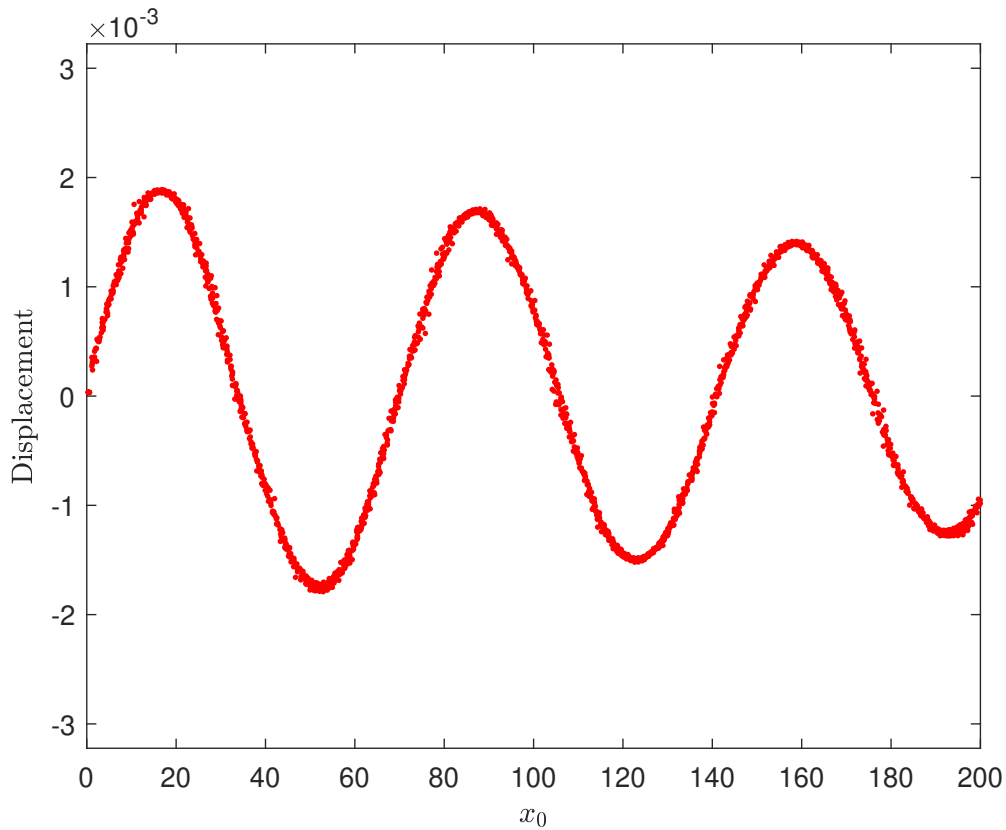


Figure 4.6. Snapshot of Simulation for Overpressurized System

wave across the figure, the particles are no longer tightly constrained to the waveform. We can see a large amount of the non-affine motion discussed in Chapter 1. Additionally we can see a number of 'rattlers', particles that are barely moving at all and therefore not having as large of an impact on the backbone.

These low-pressure effects also have bearing on the attenuation and dispersion results. Figures 4.8 and 4.9 show the attenuation and dispersion results respectively for the 2D simulations. Three different pressures were used with the same 5 seed numbers for each pressure. The points on the graph are the average of the five seeds for that given data set, with error bars to show the deviation between seeds. Additionally, the colors show three different initial pressures with pressure increasing from blue to green to red. Similar to the previous attenuation and dispersion graphs, the one dimensional theory from Eqs. (2.4) and

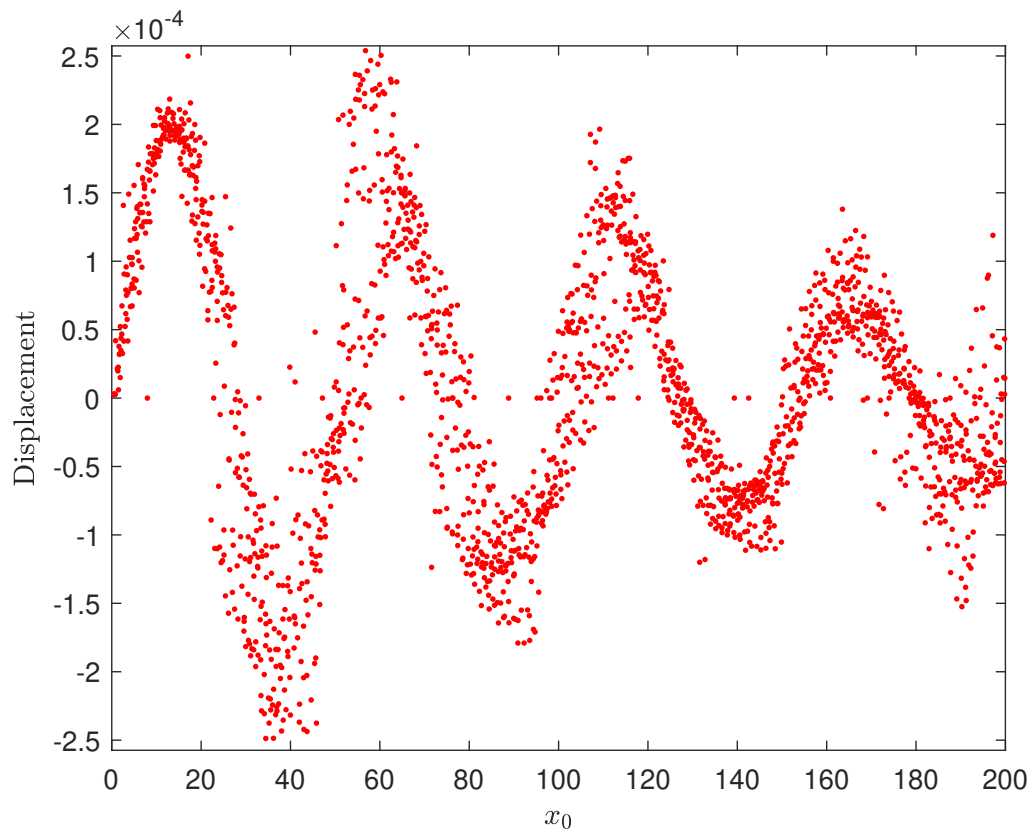


Figure 4.7. Snapshot of Simulation for Underpressurized System

(2.5) are plotted as a point of reference. Additionally, the theory curves for each color have been shifted slightly to show a rough approximation of how the various pressures align with shifted versions of this curve.

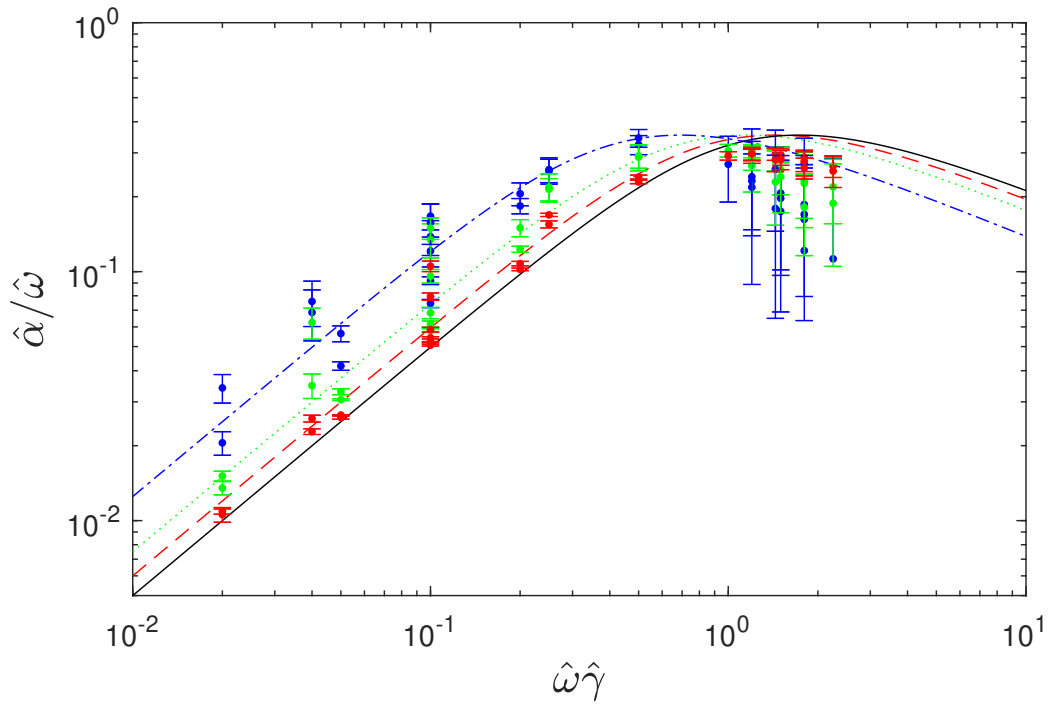


Figure 4.8. Attenuation Results for 2D Simulations

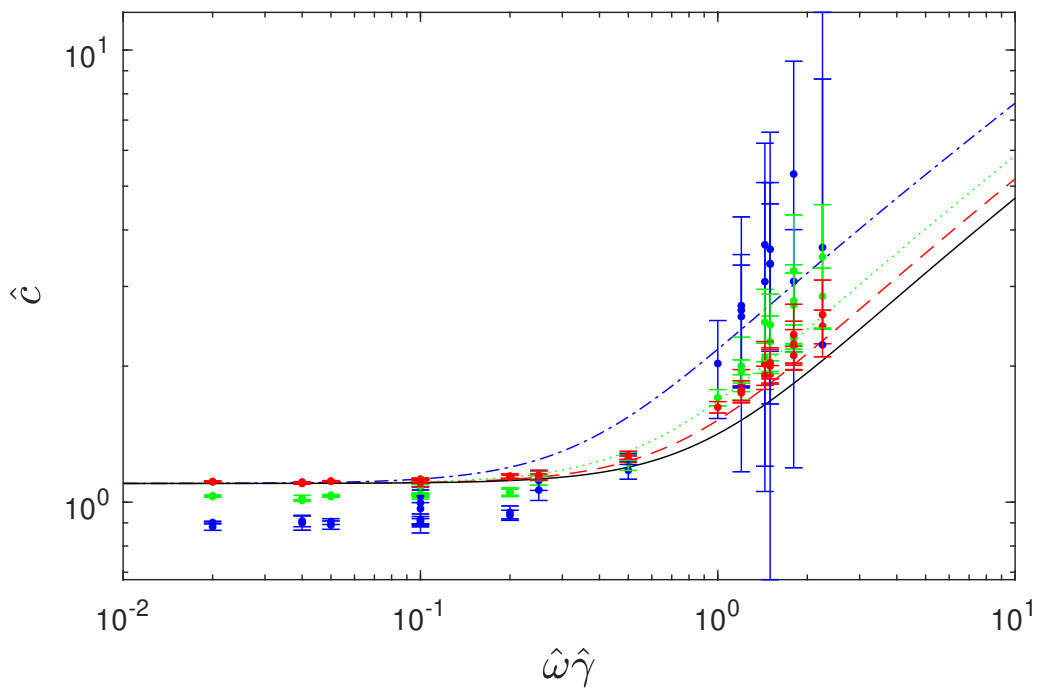


Figure 4.9. Dispersion Results for 2D Simulations

A few interesting characteristics can be noted. Looking first at the attenuation relationship we can see that lower system pressure results in higher attenuation as well as a crossover value of $\hat{\omega}\hat{\gamma}$ that decreases below 1. Mathematically, this effect, which is responsible for shifting the red, green, and blue theory curves shown in the figures, is equivalent to increasing the effective dashpot value as frequency decreases. We hypothesize that this is due to larger relative velocities for lower pressures, leading to more dissipation for a given dashpot magnitude, due to increasing non-affine motion of particles at lower system pressures. More significant non-affine motion is a hallmark of systems near the (un)jamming transition, as discussed in the introduction. This is an inherently granular effect that highlights the importance of our approach. At higher values of $\hat{\omega}\hat{\gamma}$ the lower pressure simulations appear to decrease faster, however there are some issues with data extraction in the higher $\hat{\omega}\hat{\gamma}$ range that make the validity of some of this data questionable at high frequencies.

Shifting attention to the dispersion relationships in Figure 4.9 we can see that one again there is a difference between each of the pressures. In the lower frequency range, the lower pressures result in lower wave speed, however with increasing $\hat{\omega}\hat{\gamma}$ we see that the lower pressure simulations have wave speeds that rise at a faster rate than the higher pressurized systems. However, the error bars become increasingly larger as well in this region. We once again struggle with having few data points which leads to a less collapsed curve.

4.5 Conclusions

The results that have been achieved from the simulations thus far are promising. We have managed to validate that we can get results back from one dimensional simulations that match the one dimensional theory. Additionally we have already started to see the impact of higher order effects with the 2D simulations. There is room for improvement in the 2D simulations particularly in regions of higher $\hat{\omega}\hat{\gamma}$, as well as an assessment of what is causing the frequency envelope seen in Figure 5.1. Current data extraction methods do appear to work but can be improved upon as well.

CHAPTER 5: Conclusions

This thesis has sought to better understand the dispersion relations of acoustic waves in the marine environment, particularly in regards to waves propagating through marine sediment. While existing theories have certain strengths and can be fit to data, this strictly granular approach focusing on grain-grain forces shows promise. We developed theoretical equations (Eq. (2.5) and (2.4)) for the wave speed ratio and attenuation as a function of the wave's frequency using one simple fit parameter, $\hat{\gamma}$. These theoretical equations were validated using 1D simulations that utilized a simple chain of identical grains. An expansion of the simulations to 2D allowed for further insights into the impacts of higher order effects similar to those discussed in Section 1.4. Further expansion of the 2D simulations and refinement of the 2D data extraction methods should yield additional insights into the impacts of these higher order effects, and possible ways to quantitatively determine the impact of various system initial conditions.

5.1 Future Work

Continuing to improve the data extraction methods utilized for the 2D simulations will allow for further insights into what is happening during the simulations. In particular, there is one additional effect apparent when watching the plots of the simulations progressing in real time. While the wave exists at the driving frequency, ω , other frequencies are noticeable as well. This can be seen in Figure 5.1. Each plot shows the history of a particle's position throughout the life of the simulation. While there is the underlying wave at the driving frequency, a lower frequency envelope changes what should be a relatively constant amplitude for these waves. This effect is one that we do not fully understand and will therefore require additional research on future projects.

The end of the previous chapter highlighted two of the main areas that additional work on this problem can be done. First and foremost, additional approaches need to be considered to better extract data from the simulations with high $\hat{\omega}\hat{\gamma}$ so that results can be better collapsed and therefore better understood. Capturing data in a way that allows for evaluation in the

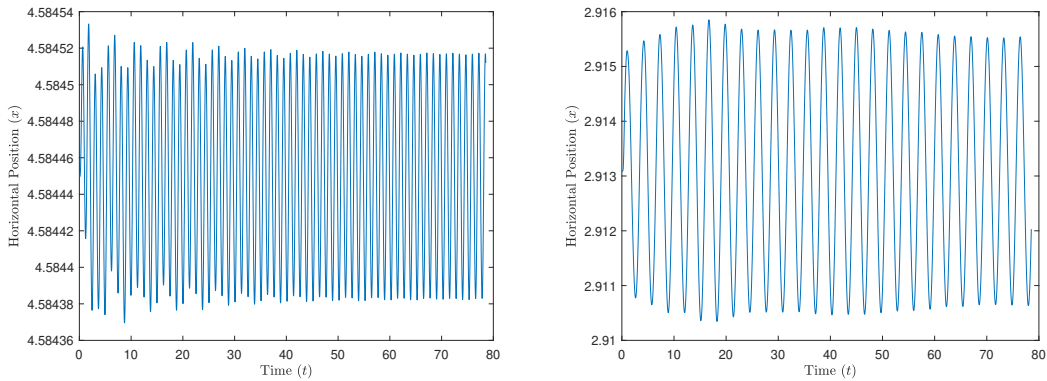


Figure 5.1. Particle Positions vs. Time in 2D Simulations

frequency domain vice just the time and spatial domains will be vital to further understanding this. Currently there are two noticeable effects, first being the envelope on the waveform present in Fig. 5.1 that was discussed in the previous chapter. Additionally, we can see a sinusoidal component to the peaks that are being fit to determine the attenuation, $\hat{\alpha}$. One example of this is shown in Fig. 5.2. In this figure we can see a spatial frequency that follows the decay down. Developing better data processing in the frequency domain could allow for substantially further understanding of these effects.

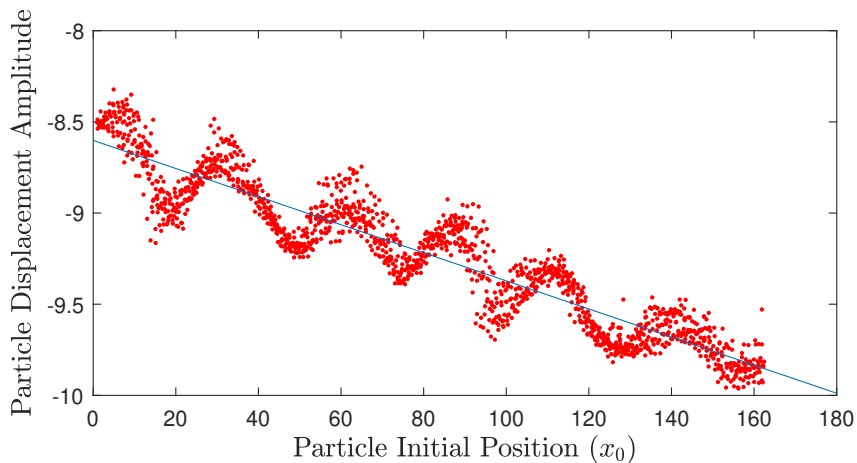


Figure 5.2. Particle Displacement Amplitudes vs. Initial Positions

Additionally evaluating the impact of system pressurization in a more quantitative way

could provide the means to predict how the pressure is impacting the results and allow for further collapsing of each of those curves onto one curve. While we roughly plotted curves on Figs. 4.9 and 4.8 to overlay some of the differences in the various system pressures, developing a quantitative understanding of these effects is another piece of the puzzle.

Beyond those issues, the final obvious step is to expand to 3 dimensions and see what changes from the 2D simulations and results. Seeing what new effects emerge in this higher dimension will provide insights into when and how this approach to marine sediment acoustics is valid.

5.2 Closing Remarks

Approaching marine sediment dispersion relations as a granular problem appears to be a promising line of research. The use of this granular based loss mechanism could drastically simplify our approach to and understanding of this problem. In turn, this could be used to improve U.S. Naval technology and further our ability to operate in a wide variety of acoustic environments.

THIS PAGE INTENTIONALLY LEFT BLANK

List of References

- [1] O. A. Godin, “Effects of weak shear rigidity of the seabed on sound propagation in a range-dependent ocean,” *The Journal of the Acoustical Society of America*, vol. 153, no. 3_supplement, p. A86, Mar. 2023 [Online]. Available: <https://doi.org/10.1121/10.0018259>
- [2] K. L. Gemba, H. J. Vazquez, J. Sarkar, B. Cornuelle, W. S. Hodgkiss, and W. A. Kuperman, “Moving ship tomography in the Santa Barbara Channel Experiment 2016,” *The Journal of the Acoustical Society of America*, vol. 146, no. 4_Supplement, p. 2858, Oct. 2019 [Online]. Available: <https://doi.org/10.1121/1.5136919>
- [3] Y. Jiang, B. Katsnelson, and O. A. Godin, “Observations of noise due to nonlinear internal waves in the ASIAEX experiment in the South China Sea,” *The Journal of the Acoustical Society of America*, vol. 152, no. 4, p. A212, Oct. 2022 [Online]. Available: <https://doi.org/10.1121/10.0016044>
- [4] F. Meyer and K. L. Gemba, “Probabilistic focalization for shallow water localization,” *The Journal of the Acoustical Society of America*, vol. 150, no. 2, pp. 1057–1066, Aug. 2021 [Online]. Available: <https://doi.org/10.1121/10.0005814>
- [5] E. T. Owens and K. E. Daniels, “Sound propagation and force chains in granular materials,” *Europhysics Letters*, vol. 94, no. 5, p. 54005, May 2011 [Online]. Available: <https://doi.org/10.1209/0295-5075/94/54005>
- [6] Y. Shang *et al.*, “Research progress in distributed acoustic sensing Techniques,” *Sensors*, vol. 22, no. 16, p. 6060, Jan. 2022. Number: 16 Publisher: Multidisciplinary Digital Publishing Institute [Online]. Available: <https://doi.org/10.3390/s22166060>
- [7] T. W. Tan and O. A. Godin, “Ambient sound directionality and rapid estimation of empirical Green’s functions in a coastal ocean,” *The Journal of the Acoustical Society of America*, vol. 152, no. 4, p. A153, Oct. 2022 [Online]. Available: <https://doi.org/10.1121/10.0015861>
- [8] D. R. Olson, “The effect of seafloor roughness on passive estimates of the seabed reflection coefficient,” *The Journal of the Acoustical Society of America*, vol. 153, no. 1, pp. 586–601, Jan 2023 [Online]. Available: <https://doi.org/10.1121/10.0016846>
- [9] D. R. Olson and A. P. Lyons, “Resolution dependence of rough surface scattering using a power law roughness spectrum,” *The Journal of the Acoustical Society of*

America, vol. 149, no. 1, pp. 28–48, jan 2021 [Online]. Available: <https://doi.org/10.1121/10.0002974>

- [10] A. P. Lyons, D. R. Olson, and R. E. Hansen, “Modeling the effect of random roughness on synthetic aperture sonar image statistics,” *The Journal of the Acoustical Society of America*, vol. 152, no. 3, pp. 1363–1374, sep 2022 [Online]. Available: <https://doi.org/10.1121/10.0013837>
- [11] C. W. Holland *et al.*, “Seabed structure inferences from TREX13 reflection measurements,” *IEEE Journal of Oceanic Engineering*, vol. 42, no. 2, pp. 268–288, apr 2017 [Online]. Available: <https://doi.org/10.1109/joe.2017.2658418>
- [12] D. Jackson and D. R. Olson, “The small-slope approximation for layered, fluid seafloors,” *The Journal of the Acoustical Society of America*, vol. 147, no. 1, pp. 56–73, 2020 [Online]. Available: <https://doi.org/10.1121/10.0000470>
- [13] D. R. Olson and D. Jackson, “Scattering from layered seafloors: Comparisons between theory and integral equations,” *The Journal of the Acoustical Society of America*, vol. 148, no. 4, pp. 2086–2095, oct 2020 [Online]. Available: <https://doi.org/10.1121/10.0002164>
- [14] J.-X. Zhou, X.-Z. Zhang, and D. P. Knobles, “Low-frequency geoacoustic model for the effective properties of sandy seabottoms,” *The Journal of the Acoustical Society of America*, vol. 125, no. 5, pp. 2847–2866, May 2009. Publisher: Acoustical Society of America [Online]. Available: <https://doi.org/10.1121/1.3089218>
- [15] K. E. Gilbert, “Reflection of sound from a randomly layered ocean bottom,” *The Journal of the Acoustical Society of America*, vol. 68, no. 5, pp. 1454–1458, nov 1980 [Online]. Available: <https://doi.org/10.1121/1.385112>
- [16] K. E. Gilbert, “A propagator matrix method for periodically stratified media,” *The Journal of the Acoustical Society of America*, vol. 73, no. 1, pp. 137–142, jan 1983 [Online]. Available: <https://doi.org/10.1121/1.388847>
- [17] C. W. Holland, P. L. Nielsen, J. Dettmer, and S. Dosso, “Resolving meso-scale seabed variability using reflection measurements from an autonomous underwater vehicle,” *The Journal of the Acoustical Society of America*, vol. 131, no. 2, pp. 1066–1078, feb 2012 [Online]. Available: <https://doi.org/10.1121/1.3672696>
- [18] J. Belcourt, C. W. Holland, S. E. Dosso, J. Dettmer, and J. A. Goff, “Depth-dependent geoacoustic inferences with dispersion at the New England Mud Patch via reflection coefficient inversion,” *IEEE Journal of Oceanic Engineering*, vol. 45, no. 1, pp. 69–91, jan 2020 [Online]. Available: <https://doi.org/10.1109/joe.2019.2900115>

- [19] J. Dettmer, S. E. Dosso, and C. W. Holland, “Trans-dimensional geoacoustic inversion,” *The Journal of the Acoustical Society of America*, vol. 128, no. 6, pp. 3393–3405, dec 2010 [Online]. Available: <https://doi.org/10.1121/1.3500674>
- [20] M. Biot, “Theory of propagation of elastic waves in a fluid-saturated porous solid. I. Low-frequency range,” *The Journal of the Acoustical Society of America*, June 2005 [Online]. Available: <https://pubs.aip.org/asa/jasa/article/28/2/168/737238/Theory-of-Propagation-of-Elastic-Waves-in-a-Fluid>
- [21] M. A. Biot, “Theory of propagation of elastic waves in a fluid-saturated porous solid. II. Higher frequency range,” *The Journal of the Acoustical Society of America*, vol. 28, no. 2, pp. 179–191, June 2005 [Online]. Available: <https://doi.org/10.1121/1.1908241>
- [22] M. A. Biot, “Generalized theory of acoustic propagation in porous dissipative media,” *The Journal of the Acoustical Society of America*, vol. 34, no. 9A, pp. 1254–1264, July 2005 [Online]. Available: <https://doi.org/10.1121/1.1918315>
- [23] R. D. Stoll, “Acoustic waves in ocean sediments,” *GEOPHYSICS*, vol. 42, no. 4, pp. 715–725, June 1977. Publisher: Society of Exploration Geophysicists [Online]. Available: <https://doi.org/10.1190/1.1440741>
- [24] R. D. Stoll, “Theoretical aspects of sound transmission in sediments,” *The Journal of the Acoustical Society of America*, vol. 68, no. 5, pp. 1341–1350, Nov. 1980 [Online]. Available: <https://doi.org/10.1121/1.385101>
- [25] R. D. Stoll and T. [U+FFFD]an, “Reflection of acoustic waves at a water–sediment interface,” *The Journal of the Acoustical Society of America*, vol. 70, no. 1, pp. 149–156, July 1981 [Online]. Available: <https://doi.org/10.1121/1.386692>
- [26] R. D. Stoll, “Marine sediment acoustics,” *The Journal of the Acoustical Society of America*, vol. 77, no. 5, pp. 1789–1799, May 1985 [Online]. Available: <https://doi.org/10.1121/1.391928>
- [27] A. L. Bonomo and M. J. Isakson, “A comparison of three geoacoustic models using bayesian inversion and selection techniques applied to wave speed and attenuation measurements,” *The Journal of the Acoustical Society of America*, vol. 143, no. 4, pp. 2501–2513, apr 2018 [Online]. Available: <https://doi.org/10.1121/1.5032205>
- [28] M. J. Buckingham, “Theory of acoustic attenuation, dispersion, and pulse propagation in unconsolidated granular materials including marine sediments,” *The Journal of the Acoustical Society of America*, vol. 102, no. 5, pp. 2579–2596, 1997 [Online]. Available: <https://doi.org/10.1121/1.420313>

- [29] M. J. Buckingham, “Wave propagation, stress relaxation, and grain-to-grain shearing in saturated, unconsolidated marine sediments,” *The Journal of the Acoustical Society of America*, vol. 108, no. 6, pp. 2796–2815, Dec. 2000 [Online]. Available: <https://doi.org/10.1121/1.1322018>
- [30] M. J. Buckingham, “On pore-fluid viscosity and the wave properties of saturated granular materials including marine sediments,” *The Journal of the Acoustical Society of America*, vol. 108, no. 6, Sep. 2007 [Online]. Available: <https://pubs.aip.org/asa/jasa/article/122/3/1486/853009/On-pore-fluid-viscosity-and-the-wave-properties-of>
- [31] C. F. Schreck, T. Bertrand, C. S. O’Hern, and M. D. Shattuck, “Repulsive contact interactions make jammed particulate systems inherently nonharmonic,” *Phys. Rev. Lett.*, vol. 107, p. 078301, Aug 2011 [Online]. Available: <https://doi.org/10.1103/PhysRevLett.107.078301>
- [32] M. van Hecke, “Jamming of soft particles: Geometry, mechanics, scaling and iso-staticity,” *Journal of Physics: Condensed Matter*, vol. 22, no. 3, p. 033101, 2009.
- [33] M. Wyart, L. E. Silbert, S. R. Nagel, and T. A. Witten, “Effects of compression on the vibrational modes of marginally jammed solids,” *Phys. Rev. E*, vol. 72, p. 051306, Nov 2005 [Online]. Available: <https://doi.org/10.1103/PhysRevE.72.051306>
- [34] L. E. Silbert, A. J. Liu, and S. R. Nagel, “Vibrations and diverging length scales near the unjamming transition,” *Phys. Rev. Lett.*, vol. 95, p. 098301, Aug 2005 [Online]. Available: <https://doi.org/10.1103/PhysRevLett.95.098301>
- [35] J. Schäfer, S. Dippel, and D. Wolf, “Force schemes in simulations of granular materials,” *Journal de Physique I*, vol. 6, 01 1996 [Online]. Available: <https://doi.org/10.1051/jp1:1996129>
- [36] A. H. Clark, E. E. Brodsky, H. J. Nasrin, and S. E. Taylor, “Frictional weakening of vibrated granular flows,” *Phys. Rev. Lett.*, vol. 130, p. 118201, Mar 2023 [Online]. Available: <https://doi.org/10.1103/PhysRevLett.130.118201>
- [37] K. E. Daniels, J. E. Kollmer, and J. G. Puckett, “Photoelastic force measurements in granular materials,” *Review of Scientific Instruments*, vol. 88, no. 5, p. 051808, May 2017 [Online]. Available: <https://doi.org/10.1063/1.4983049>
- [38] S. L. Garrett, *Understanding Acoustics*. Springer International Publishing, 2020 [Online]. Available: <https://doi.org/10.1007/978-3-030-44787-8>
- [39] M. V. Shitikova and A. I. Krusser, “Models of viscoelastic materials: a review on historical development and formulation,” *Theoretical Analyses, Computations, and*

Experiments of Multiscale Materials: A Tribute to Francesco dell'Isola, pp. 285–326, 2022.

- [40] N. S. Martys and R. D. Mountain, “Velocity verlet algorithm for dissipative-particle-dynamics-based models of suspensions,” *Phys. Rev. E*, vol. 59, pp. 3733–3736, Mar 1999 [Online]. Available: <https://doi.org/10.1103/PhysRevE.59.3733>

THIS PAGE INTENTIONALLY LEFT BLANK

Initial Distribution List

1. Defense Technical Information Center
Ft. Belvoir, Virginia
2. Dudley Knox Library
Naval Postgraduate School
Monterey, California



DUDLEY KNOX LIBRARY

NAVAL POSTGRADUATE SCHOOL

WWW.NPS.EDU

WHERE SCIENCE MEETS THE ART OF WARFARE